nuclear fusion
IAEA

PAPER • OPEN ACCESS

Tritium production and processing systems for ST-E1

To cite this article: E. Yildirim *et al* 2026 *Nucl. Fusion* **66** 086004

View the article online for updates and enhancements.

You may also like

- Integrated physics and magnet design for the ST-E1 fusion power plant
E.N.J. Maartensson, N. Welch, M. Scarpari et al.
- Power and particle exhaust in the ST-E1 fusion power plant
M. Robinson, A. Scarabosio, E. Vekshina et al.
- Results from the last DD and DT JET campaigns in the framework of the EUROfusion Tokamak Exploitation Work Package activity
N. Vianello, E. Joffrin, M. Baruzzo et al.

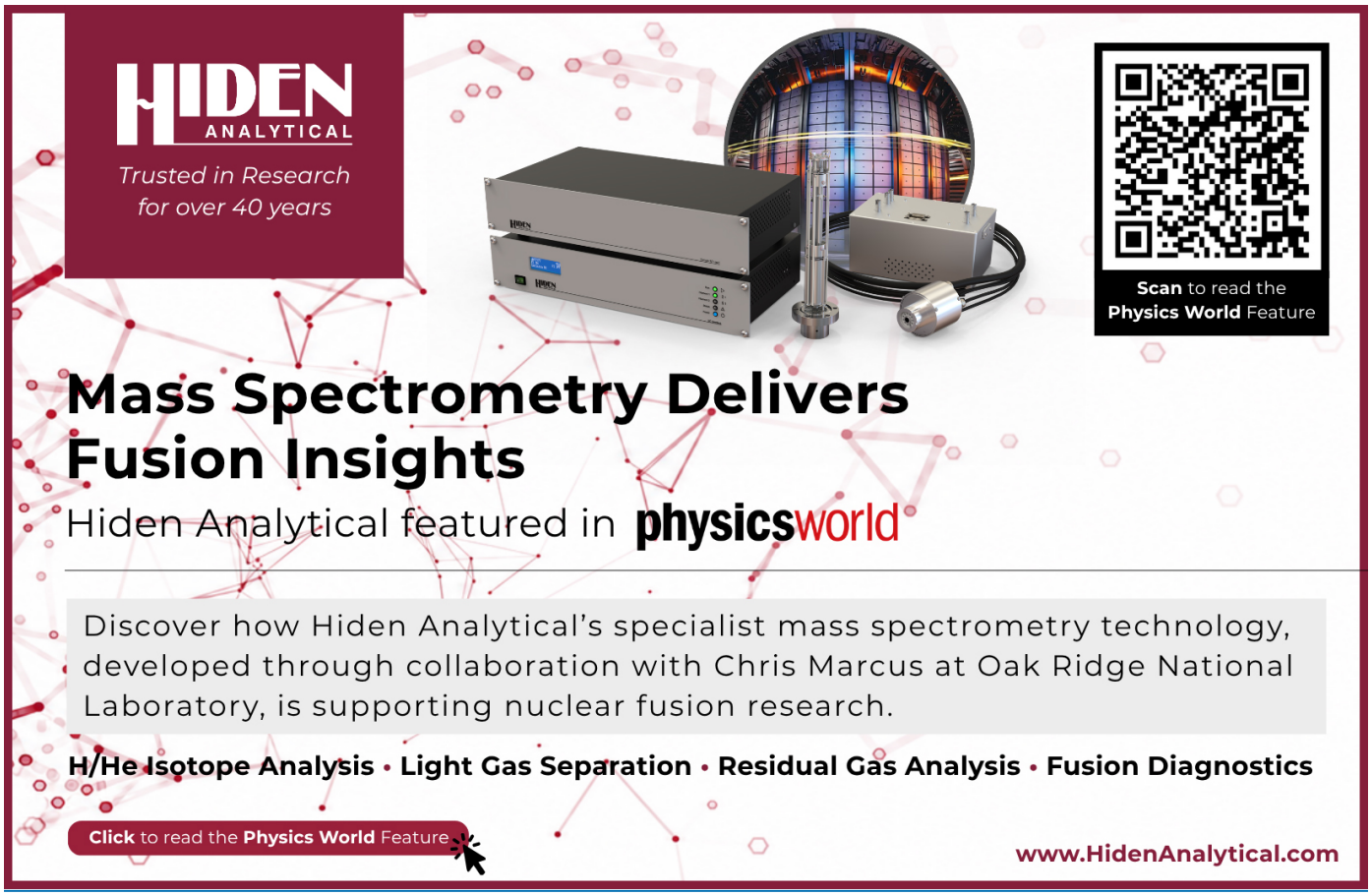

This content was downloaded from IP address 130.51.23.114 on 03/11/2026 at 03:04

OPEN ACCESS
IOP Publishing | International Atomic Energy Agency Nuclear Fusion
Nucl. Fusion **66** (2026) 086004 (25pp) https://doi.org/10.1088/1741-4326/ae773a

Tritium production and processing systems for ST-E1

E. Yildirim[1,*], J. Naish[1], J. Trueba[1], S. Levine[1], A. Kumar[1], V.B. Gohani[1], M.K.E. Mohamed[1], A. Vorobev[1], L. Yang[2], P.C. Simon[2,3], A. Somers[4], C. Malone[4], H. Flynn[4], P. Rowell[4], T. Stahl[4], G.K. Larson[4], R. Barnett[5], L.R. Baylor[5], T.E. Gebhart[5] and N. Adhikari[5]

[1] Tokamak Energy Ltd, Milton Park, Oxfordshire, United Kingdom of Great Britain and Northern Ireland
[2] Idaho National Laboratory (INL), Idaho Falls, ID, United States of America
[3] Ken and Mary Alice Lindquist Department of Nuclear Engineering, The Pennsylvania State University, University Park, PA 16802, United States of America
[4] Savannah River National Laboratory (SRNL), Aiken, SC, United States of America
[5] Oak Ridge National Laboratory (ORNL), Oak Ridge, TN, United States of America

E-mail: e.m.yildirim97@tokamakenergy.com

Received 18 December 2025, revised 18 May 2026
Accepted for publication 3 June 2026
Published 10 July 2026

Abstract

An integrated tritium fuel-cycle architecture has been developed for ST-E1, a low-aspect-ratio, high-power fusion power plant. The approach couples a helium-cooled liquid-lithium breeder blanket with a dedicated circulation loop providing tritium extraction, heat removal, and inventory control within a unified system boundary. Downstream of the blanket, the tritium processing system comprises of extraction, purification, isotope separation, and storage subsystems sized to accommodate the plant's dynamic tritium production and consumption rates. Inventory modelling is used to assess candidate extraction schemes, evaluate tritium residence and holdup, and quantify sensitivities associated with protium control and intermediate inventories. The integrated assessment indicates that the combined blanket-processing architecture can satisfy startup and steady-state tritium requirements within credible operating margins, with a low overall inventory and acceptable doubling time. The results identify tritium extraction sensitivity and fuelling efficiency as the dominant drivers of inventory performance, rather than marginal improvements in breeding ratio. Overall, the analysis demonstrates the feasibility of a self-consistent fuel cycle for ST-E1 and highlights the critical dependencies between blanket inventory management, processing throughput, and overall plant performance.

Supplementary material for this article is available online

Keywords: tritium fuel cycle, lithium blanket, DIR fraction, isotope separation, ST-E1

(Some figures may appear in colour only in the online journal)

* Author to whom any correspondence should be addressed.

Original content from this work may be used under the terms of the Creative Commons Attribution 4.0 licence. Any further distribution of this work must maintain attribution to the author(s) and the title of the work, journal citation and DOI.

1. Introduction

Continuous tritium production and fuel recycling in fusion power plants is critical for sustained and commercially viable fusion energy. Tokamak Energy's ST-E1 [1] represents an upgradable Fusion Power Plant with a significant pilot operating phase enabling the de-risking and optimisation of critical subsystems. The ST-E1 tokamak itself is a low aspect ratio tokamak pushing for steady state operation, meaning fuel production and processing are key elements for the viability of this pre-conceptual design. In the pilot phase, there is no requirement for significant tritium production. Instead, tritium production must compensate for losses due to radioactive decay and internal processing within the fuel cycle, in addition to that burnt within the fusion reaction. With this in mind, the major features that must be considered are: tritium production to cover these losses, tritium processing to resupply fuel in appropriate compositions, and overall tritium behaviour across the plant to understand the initial startup inventory requirement and self-sufficiency.

The design of these systems is based on the ST-E1 reference operating point defined in [1, 2], corresponding to a device with a fusion power of 1573 MW and an aspect ratio of 2.3. The low-aspect-ratio configuration imposes distinctive design constraints, as the geometry of the central column predominantly determines the overall radial build of the device. The resultant spatial restrictions inhibit the implementation of inboard tritium breeding, thereby posing a challenge to achieving an adequate tritium breeding ratio (TBR). Consequently, an outboard-only breeding strategy has been adopted, implemented within a removable segment[6] illustrated in figure 1. Furthermore, the high fusion power level necessitates highly efficient fuelling and tritium processing systems in order to minimise both start-up and steady-state tritium inventories.

This paper presents the first end-to-end, internally consistent fuel-cycle baseline for ST-E1. It contains analysis of tritium production—including breeding blanket, supporting lithium systems and safety (section 2); tritium processing—fuel supply and plasma exhaust, fast-rebalancing subsystem tritium loss and tritium safety (section 3); and a final integrated plant-wide tritium transport and inventory modelling encompassing these elements (section 4).

Four principal drivers govern the feasibility of the proposed design. Specifically, assessment of whether a pre-concept ST-E1 fuel-cycle architecture can: (i) fuel and exhaust the plasma with credible pumping margins and fuelling efficiencies; (ii) rapidly rebalance the fuel inventory while satisfying a $\leqslant 0.8$ at.% (atomic percentage) protium requirement for direct internal recycling (DIR); (iii) address the technical challenges and exploit the potential advantages associated with a liquid-lithium blanket system; and (iv) achieve tritium self-sufficiency with acceptable start-up and steady-state component inventories, explicitly accounting for key losses, including those potentially occurring in the plasma-facing components (PFCs). Together, these quantitatively establish boundaries on performance metrics, identify dominant design drivers, and delineate the associated risks and technology development priorities that will be carried forward into the conceptual design phase. The conclusions of this paper offer the first measurement of ST-E1's fuel cycle against these drivers.

[6] The concept of a removable segment, intended to facilitate both maintenance and upgrades, is discussed in detail in [3].

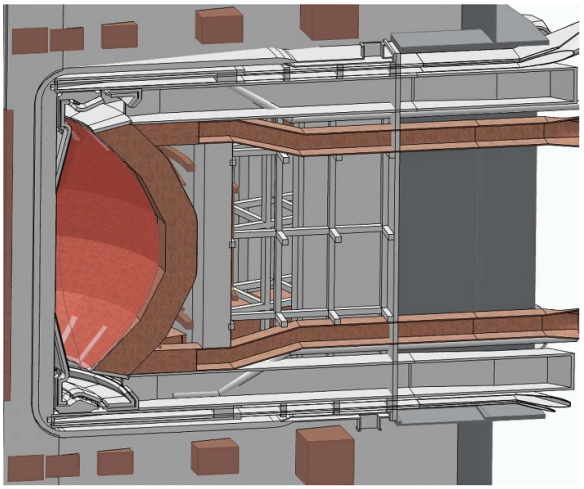

Figure 1. ST-E1 showing the removable segment with the breeder blanket highlighted, inclusive of the lithium pipes. The breeder material enters at the bottom of the duct, and is heated as it moves to the outlet pipe at the top of the blanket.

2. Tritium production

The fuel cycle of any fusion device is critically dependent on the selection of the breeder material, which in turn determines the configuration of the lithium-based subsystems that make up the overall lithium loop. For ST-E1, an initial design target for the TBR is set to 1.20 for rough scoping studies. In these studies geometries are more coarse, and further design iterations and increased modelling fidelity typically lead to a decrease in the achievable TBR. This target is based on an assumed maximum reduction of 0.20 in TBR, of which approximately 0.05 is attributed to uncertainties in nuclear data, deeper geometric and engineering design, modelling approximations, and additional tritium losses. Under these assumptions, the resulting TBR is expected to remain at or above unity.

An initial simulation of the TBR using literature systems [4–8], in addition to novel concepts with a Monte Carlo neutron transport code, OpenMC [9], was performed. The geometry used can be seen in figure 1. The analysis performed here included the effect of this more detailed structure, including the effects of surrounding materials such as the shielding and surrounding structural materials. The results are presented in table 1. These studies show that only solid breeders and natural lithium achieve the target TBR in excess of 1.20. When considering the requirement for high isotopic enrichment of solid breeders, their dependence on toxic and costly beryllium [10], and unresolved issues concerning the crush resistance [11, 12],

Table 1. table of breeder options and their resultant neutronics characteristics: TBR and energy multiplication (EM) for ST-E1's geometry.

	Liquid breeders			Solid breeders	
Name	$Li_{17}Pb_{83}$	Li	FliBe	Li_4SiO_4	Li_2TiO_3
Description	Eutectic lithium lead	Liquid lithium	Liquid lithium salt	Lithium orthosilicate	Lithium titanate
Multiplier	Pb	Li	Be	Be	Be
Enrichment	90%	Natural	natural or enriched	50%	50%
Structural material					
TBR	1.04	1.26	0.92	1.27	
EM	0.9	0.89	0.88	1.07	

natural liquid lithium emerges as the preferred breeder material among the final shortlisted options, with further details on neutronics simulations in Chandrasekhar *et al* [13].

The remainder of this section, therefore, concentrates on the preliminary design of a liquid lithium-based breeder blanket, including key material interaction phenomena (section 2.1), the principal supporting systems and their influence on tritium behaviour within the plant (section 2.2), and the safety considerations specific to liquid lithium systems (section 2.3).

2.1. Natural lithium breeder blanket

The pure lithium blanket design progresses through assessment of compatible materials, tritium retention, effects on thermodynamic efficiency, and magnetohydrodynamics (MHD) effects, with these design parameters culminating in a reassessment of the TBR with higher fidelity. A further requirement on the structural material is limiting the neutron absorption by the structural material (for example (n,α) interactions [14]). Two key materials have been considered for use in ST-E1: reduced activation ferritic/martensitic steels (RAFM) and Vanadium-based alloys; specifically V-4Cr-4Ti (V44). V44 has superior high temperature corrosion resistance to liquid lithium compared to RAFM steels. From operational experience of other nuclear systems, a corrosion rate of less than 5 μm yr^{-1} is generally recommended for structural materials [15]. For comparison, a corrosion rate of less than 1 μm yr^{-1} has been observed in a V44 thermal convection flow loop that was run at 700 °C for 2355 h with lithium flow rates of 2–3 cm s^{-1} [16]. Minimal degradation of mechanical properties was also reported. By contrast, a corrosion rate of $\sim$15 μm yr^{-1} has been estimated for ferritic martensitic steels in 5 cm s^{-1} flowing lithium at 600 °C [8, 15]. Based on its corrosion rate in liquid lithium, the operation of RAFM steels is likely to be limited to <500–600 °C while vanadium alloys can be utilised up to 650–700 °C [17], especially with the likely blanket flow velocities being $\leqslant$1 cm s^{-1} in the majority of the blanket. The 14 MeV neutron absorption cross sections of Fe and V, respectively, critically affect the overall TBR of any breeder blanket. The lower total absorption cross section of V compared to Fe means low activation vanadium-based alloys are generally more neutron transparent compared to RAFM steels.

The tritium retention properties of the structural material should also be considered when comparing material choices, as this will factor into tritium losses and impact tritium self-sufficiency. Vanadium has a much higher solubility for hydrogen compared to iron [18, 19]. However, in the vanadium-lithium-hydrogen system, the hydrogen distribution coefficient, which reflects the ratio of hydrogen solubility in vanadium to that in liquid lithium is $\approx 10^{-2}$ at breeder blanket relevant temperatures [18] (0.0098 and 0.019 at 700 and 800 K respectively) and the flux would be dominated mass transfer in the lithium due to the slow diffusivity. Retention in the structure would increase, though, with irradiation damage, even if the thermodynamics quantities are unaffected with this requiring more detailed study in vanadium alloy to understand trapping density and depth. As a result, the concentration of tritium that partitions into a vanadium alloy structure from the lithium is not expected to significantly affect the inventory of tritium available for extraction or the lifetime of the vanadium structural material for the blanket lifetime.

The choice of structural material heavily impacts the thermodynamic efficiency of the breeder blanket as it constrains the component's allowable temperature operating window. For candidate structural materials, the lower allowable temperature is generally determined by low temperature hardening and embrittlement, while the upper temperature window is determined by either (i) thermal creep and creep-fatigue coupling, (ii) coolant or breeder compatibility, (iii) void swelling, or (iv) high temperature helium embrittlement [17]. While RAFM steels are constrained to an operating window of 350 °C–550 °C [20], V44 offers the widest temperature window of all candidate low activation structural materials in a liquid lithium breeding environment: $\sim$400 °C–700 °C [17]. An upper temperature limit of 700 °C is imposed for V44 based on creep deformation rates [17]. The ability of V44 to withstand high service temperatures importantly reduces the cooling requirement on the breeder blanket structure. This data culminates in the alloy selected as the breeder blanket structural material for ST-E1 as V-4Cr-4Ti (V44), with the specific composition originating from its reasonable technical readiness level to support concept design. The development of V44 was originally driven by the U.S. fusion power programme in the 1980s and 1990s when a self-cooled Li/V blanket was a leading concept for the U.S. ITER test blanket module [21]. As a result, there are reasonable amounts of data that demonstrate the critical material properties of V44 at relevant temperatures and conditions, its industrial scale manufacturability, and its weldability [22].

V44 selection further affects liquid lithium flow characteristics. Lithium's high electrical conductivity, along

with V44 being a conductor, means that MHD effects must be accounted for in both both poloidal and toroidal components of the magnetic field. More critical is the toroidal component, which principally causes so called *MHD drag* in the blanket. This limits its flow, which can lead to local hot spots, higher pumping requirements, and local accumulation of tritium. Large scale coupled MHD/CFD (computational fluid dynamics) simulations remain an area of technological development, so a full evaluation of the ability of lithium to remove heat and the potential of a self-cooled option at high Hartmann number will remain a task beyond this preconceptual phase. For initial scoping, dual cooled options have been highlighted. The secondary coolant must have efficient heat transfer, sufficient pumpability, and be compatible with the structural materials and the lithium itself. Helium was selected as the secondary coolant because it is chemically inert (no reaction with lithium compared to water or supercritical CO_2) and possesses high thermal conductivity. Two things must be noted when making this choice: the first being that the high temperature compatibility of V44 with the coolant may be problematic since the pickup of hydrogen and oxygen, which are trace impurities in helium, is known to cause matrix hardening and embrittlement. Conservative estimates suggest that the required oxygen concentration level in helium to avoid severe loss of ductility needs to be less than 1 part per billion, which may be unfeasible to achieve with current purification technology [23]. Further evaluation is needed to determine if a protective coating may be required for helium cooling channels and pipes. If so, silicide coatings (e.g. VSi_2) are a promising option [24]. The second issue encountered with the selection of helium as the blanket coolant is that there are large parasitic loads from its compression to meet the large inventory requirements likely needed for ST-E1, as shown in [25]. Overall, this leads to the breeder blanket for ST-E1 to be a dual-cooled lithium (DCLi) blanket as a baseline solution, initially assuming total heat removal of the blanket for initial analysis by helium until more detailed coupled MHD/CFD simulation has been developed. The geometry can be seen in figure 1, where lithium enters at the inlet port at the bottom of the blanket segment, and is heated as it moves to the top of the structure, leaving by the outlet port. An assessment of heat removal from the blanket can be found in the accompanying paper [25], in addition to more detail on the blanket internal structure.

With these further developments of the blanket system, the TBR can be reassessed with a higher fidelity geometry, including piping networks and structural attributes. In addition, other structures such as H&CD ports and limiters reduce the available space for breeding. To analyse this a simplified approximation of the H&CD geometries has been included in more detailed OpenMC calculations with these additions being added to the geometry in figure 1:

- *Electron Cyclotron Resonance Heating (ECRH) system representation:* To model the effect of the ECRH system on the breeder blanket, six penetrations were introduced per toroidal field (TF) segment. Each penetration was modelled with a diameter of 0.5 m and a wall thickness of 1 cm.
- *Ion cyclotron resonance heating (ICRH) system representation:* The ICRH system was represented by two rectangular blocks, each measuring 1.5 m $\times$ 2 m with a thickness of 20 cm. The material composition was defined as a mixture of 7.5% tungsten, 42.5% V44 alloy, and 50% void.

Table 2 describes the variation in TBR with different levels of segment coverage for different breeding inhibitors. From this, a range of 1.085–1.14 for the TBR inclusive of ECRH, ICRH and limiters has been derived from this more detailed geometry. This preliminary analysis demonstrates a breeder blanket compatible with the minimum requirement for TBR to allow for self-sufficiency on ST-E1.

2.2. Supporting lithium systems

The supporting lithium loop involves critical subsystems: heat exchangers, tritium extraction and lithium purification. Two of these have a large effect on tritium behaviour in ST-E1, with these being the tritium extraction system and the high surface area in the heat exchanger[7]. Lithium flows initially from the blanket through the heat exchanger, then a 20% bleed fraction is sent to the tritium extraction system, the benefits of this configuration from a thermodynamic point of view are discussed in [25]. This section assesses the effects on tritium concentration of first the method for extraction, and then loss across the heat exchanger.

Tritium extraction from pure lithium has historically been identified as a key challenge for liquid lithium blanket systems [8]. Lithium's high affinity for tritium suppresses tritium activity in the system, which reduces the thermodynamic driving force for permeation into structural materials [27]—a benefit for regulatory compliance and structural integrity. The same low tritium activity, however, works against extraction: tritium bound in solution resists release, requiring more sophisticated extraction methods that become more effective at higher tritium concentrations, rather than relying on natural thermodynamic driving forces[8].

To sustain a higher steady-state tritium concentration, a dedicated lithium loop per blanket segment has been proposed as the primary approach to reducing total lithium inventory. For a given production rate, smaller lithium volume yields a higher equilibrium concentration, improving extraction performance and reducing the time required to reach operating concentration from startup. Despite this increase, the high solubility and low diffusivity of tritium in lithium limits the corresponding rise in permeation driving force into the surrounding vanadium structure. Therefore, the system remains below concentrations at which thermodynamic effects would lead to significant losses of tritium (target loop concentration down to 100 ppb).

[7] Purification for ST-E1 will build upon the work on purification systems for IFMIF-DONES in [26].

[8] Were such systems are developed, this characteristic also improves inventory control, since tritium is only released from the lithium within the dedicated extraction system.

Table 2. Sensitivity of tritium breeding ratio (TBR) to blanket coverage reductions and component insertions. The percentage difference is relative to the baseline configuration.

Configuration	Description	TBR (Δ%)
Baseline	Full breeding coverage	1.146 (0.0%)
100% Pipes + Stiffening Plates	All pipe/stiffener intrusions included	1.113 (−2.8%)
100% Limiters	All limiter coverage applied	1.107 (−3.4%)
33% Limiters	One-third limiter coverage	1.142 (−0.4%)
100% ECRH	Full heating/current-drive ports	1.122 (−2.1%)
33% ECRH	One-third ECRH coverage	1.135 (−0.9%)
33% ECRH + 33% Limiters	Partial H&CD + partial limiters	1.135 (−1.0%)
100% ICRH	Full ICRH launch coverage	1.085 (−8.2%)
33% ICRH	One-third ICRH coverage	1.131 (−1.3%)

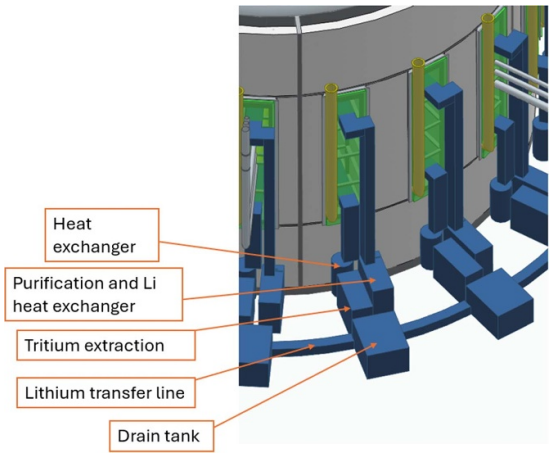

Figure 2. Figure showing the modules in the lithium loop per-segment.

This per-segment loop configuration (figure 2) reduces the total lithium mass to less than five times that contained within the blanket modules. Although beneficial, this added complexity can increase CAPEX depending on economies of scale, system design, and fabrication. The implications for total plant and startup inventories are discussed in section 4.

For tritium extraction, the LiT Electrolysis [28] method has emerged as a potential method. Electrolysis of molten lithium tritide (LiT) splits the salt into metallic lithium and molecular tritium:

$$\mathrm{LiT\,(l)} \longrightarrow \mathrm{Li\,(s/l)} + \tfrac{1}{2}\mathrm{T_2\,(g)}. \tag{1}$$

In ionic form, LiT is represented as $\mathrm{Li^+}$ and $\mathrm{T^-}$. The canonical half-reactions in a molten salt cell are:

$$\text{Cathode):} \quad \mathrm{Li^+ + e^- \rightarrow Li\,(s/l)} \tag{2}$$

$$\text{Anode:} \quad \mathrm{2T^- \rightarrow T_2\,(g) + 2e^-} \tag{3}$$

with equation (1) obtained by adding (2) and (3) and cancelling electrons.

A solid $\mathrm{Li^+}$ conductor (e.g. LLZO or related ceramics) forms a tube, disc, or plate separating the anode (molten LiT) from a lithium collection compartment. Only $\mathrm{Li^+}$ traverses the membrane; tritide remains in the anolyte and forms $\mathrm{T_2}$ at the anode, which is then sparged away. There is initial evidence that LiT electrolysis may be considered more beneficial for lower concentrations.

This system has challenges in upscale and robustness due to potential oxygen leaching into the ceramics at higher temperatures, and challenges with phase changes during long term submersion [29]. Despite this, development of such a system will be a key enabler for pure lithium based systems. Furthermore, initial sizing estimates show a low overall duty of the system for ST-E1 level lithium flows, with initial duty calculations suggesting $\leqslant 1 kW_e$ system duty, further details on these estimates are held in supplementary information A.3.

Tritium losses during heat exchange prior to extraction must be accounted for, particularly given the large surface area involved. This heat exchanger can be assumed to be a shell and tube heat exchanger, and thus a bundles of tubes. Tritium can permeate through the V44 tube walls of the lithium-helium heat exchanger. The fractional loss, η, for a bundle of tubes is given by the closed-form solution of Humrickhouse and Merrill [30]:

$$\eta = 1 - \exp\left(-\frac{\tau\zeta}{1+\zeta}\right), \tag{4}$$

where dimensionless parameters τ and ζ characterize lithium-side mass transport and tube-wall permeation, respectively. This can be used to understand the loss in the Li-He heat exchanger.

Figure 3 presents the tritium loss fraction through the Li-He heat exchanger as a function of the lithium inlet temperature, comparing the baseline configuration (tube length $L = 2.44$ m, inner diameter $d = 16.6$ mm, from [25]) with variants employing shorter/longer tubes and smaller/larger tube diameters. The current ST-E1 operating point at 588 °C yields a calculated loss fraction of $\eta \simeq 2.7 \times 10^{-4}$, whereas operation at the upper allowable temperature for the V-4Cr-4Ti structural material (700°C) increases the loss fraction to $\eta \simeq 1.4 \times 10^{-3}$, which remains well below the percent level. Further reductions in tritium losses can be achieved by increasing the lithium flow velocity, enlarging the tube diameter, or increasing wall thickness but at present, the loss values are considered reasonable. These loss values can be implemented in the plant-wide modelling in section 4 to understand their effect on the helium coolant tritium concentration.

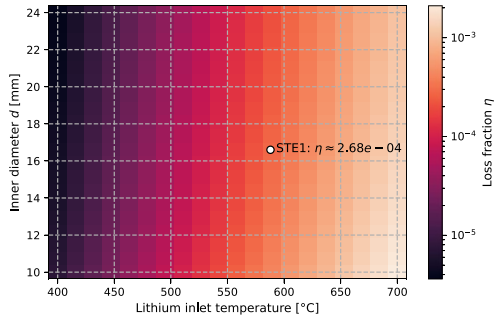

(a) Loss fraction vs. temperature and tube diameter

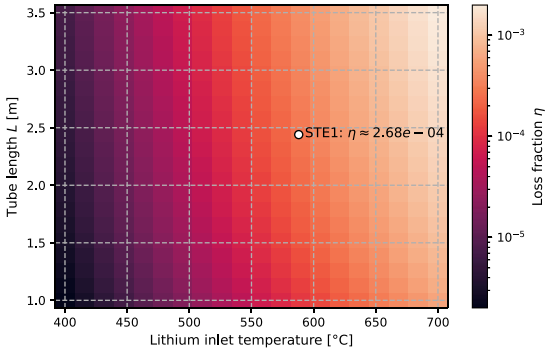

(b) Loss fraction vs. temperature and tube length

Figure 3. Tritium loss fraction η through the Li–He heat exchanger as a function of lithium inlet temperature and (*a*) tube diameter, and (*b*) tube length. The ST-E1 baseline design point is indicated in each panel.

Helium will also be produced in the blanket and has very low solubility in liquid lithium. This will naturally degas into the argon cover gas used to pressurise the loop. This passive separation means no dedicated helium removal system is required within the lithium itself. Tritium carried into the cover gas as T_2 vapour can be recovered using a palladium membrane providing clean separation. The loop operating temperature of approximately 400 °C is consistent with the standard operating range for palladium membranes [31, 32]. Should there also be He released in the electrolysis cell due to vacuum/cover gas contact (the cell reactions inherently do not involve He production), then a similar clean-up method will be utilised.

2.3. Lithium safety

For the He/Li/V breeder blanket, the dominant hazard is lithium's reaction with air and water, together with oxidation of the hot vanadium alloy. In line with the assessment in [8, 33], the blanket is only considered acceptable if credible faults cannot lead to Li or V contacting air or water. This drives the ST-E1 design choices: inerted enclosures around the blanket and primary lithium loops, exclusion of water-cooled systems from the fusion island, and separation from the steam cycle by intermediate Li→He→salt→steam loops, consistent with an Inherently Safe Design approach.

Steel liners or equivalent barriers are required around lithium systems to protect concrete and maintain confinement in spills. Lithium's high tritium solubility aids effluent control but could create a large in-blanket tritium inventory, demanding low-leak circuits and robust tritium handling. Low-activation vanadium alloys support near-surface disposal, provided impurities and accident contamination are well controlled, with this being shown in ST-E1 nuclear technology analysis in [13].

Although written for Na/NaK, ANSI/ANS-54.8 [34] offers a practical template for alkali liquid metal fire protections. These can be interpreted as an initial basis for lithium: prioritizing leak prevention and early detection, inert-gas atmospheres with oxygen monitoring, strict control of water and extinguishing agents, engineered catch pans/drains/dump tanks, and reliable, testable safety systems. This is similar to the design approach suggested in [35]. Overall, lithium safety for a Li/V blanket rests on inert, high-integrity circuits, engineered spill confinement, compatible structural protection, and tritium management developed jointly with the lithium leak and fire strategy.

3. Tritium processing

Generated and unburnt tritium must be continuously processed to allow for ST-E1 to operate. Initial sizing of these systems has been taken with a tritium burn efficiency (TBE) estimate of 1%. This value depends on the recycling coefficient of the system, which dictates the burn fraction, f_{burn}, and the fuelling efficiency, η_{f}. Combined here[9] as:

$$\text{TBE} = \eta_{\text{f}} \times f_{\text{burn}}$$

where:

- Fuelling efficiency η_{fuel}: fraction of injected fuel that is retained inside the confined plasma (post-injection losses in guides, valves, and at the edge reduce η_{fuel}).
- Burn fraction f_{burn}: fraction of the *retained* fuel that undergoes fusion.

An additional key parameter is the global recycling coefficient, R, which remains a largely unknown for burning plasmas [37]. R is correlated with the burn fraction through the effective confinement time [38]. For the given plasma conditions in the reference design case [1], achieving a TBE $= 1\%$ requires the fuelling efficiency to be 42%–26% for $0.0 \leqslant R \leqslant 0.4$.[10]

These systems within the fuel cycle can be seen in the block flow diagram in figure 4. The following sections describe studies on key systems to size them and explore key parameters. Section 3.1 focuses on fuel supply while section 3.2 focuses on plasma exhaust, exploring the effects of pellet size and pump

[9] *TBE* has also been cited elsewhere as a function of the divertor pumping behaviour [36].

[10] Further information on this relationship can be found in supplementary information A.2.

speed on the requirements in these systems. Section 3.3 goes on to discuss the fast re-balancing loop, specifically focusing on the challenges that arise from accounting for the protium percentage at the inlet. Then a final section, section 3.4, introduces a component level modelling capability that will be developed alongside the design of the PFCs, in it initial stage, to assess the retained material.

3.1. Fuel supply

The matter-injection system must supply both seeded impurities for heat-flux mitigation and DT fuel for fusion. Continuous high-field-side pellet injection [39], using frozen DT pellets, forms the baseline fuelling method here, with elucidation on the correct delivery systems for impurities to be handled in further design. The efficiency of that fuelling plays a key role in any plasma confinement system, with the high temperature pedestal in power plant scale devices being a key unknown affecting this. Solid pellets injected on the high-field side (HFS) leverage guiding-centre and $\mathbf{E}\times\mathbf{B}$ drifts to deposit material deeper after ablation [39], improving η_{f} relative to the low-field-side injection. The size of these pellets is related to plasma control. Smaller pellets at higher repetition rates are preferred to minimize density modulation and to reduce the impact of a missed pellet [40]. However, smaller pellets are less likely to penetrate into the pedestal at reactor-relevant edge temperature and density, necessitating a balance among pellet size, speed, and injection geometry.

The PELLET code [41] is used here to scan the critical parameters: pellet speed, diameter, injection point and angle for different candidate HFS injection lines (figure 5). Selection of this line early in the design protects routing space through concept and detailed phases, thereby preserving fuelling efficiency potential. A representative plasma profile and preliminary PELLET results are shown in figure 6: ablation typically peaks near the top of the pedestal, and the HFS drift enables deeper deposition. Figure 7 presents penetration-depth contours versus speed and angle from this single launch point for a 5 mm diameter spherical pellet. This initial study was used on an anticipated plasma density and temperature distribution from [42]. Table 3 shows the results of the candidate plasma profiles of the same paper and shows the height of the pedestal in terms of both density and temperature, and the final penetration values.

To corroborate drift and sensitivity trends, the HPI2 [43] and DIII-D [39] drift models, shown to agree with experimentally measured drifts in current devices, were also applied. Both models show a consistent sensitivity to the size and speed; HPI2 (Δ_{HPI2}) highlights a strong dependence on the injection angle relative to the horizontal outward direction, while the DIII-D scaling ($\Delta_{\mathrm{DIII\text{-}D}}$) does not consider injection angle. Note that there is no experimental validation on the angular variation or on reactor plasma conditions. Table 3 gives a representative summary of the penetration depths for $v_p = 1000\ \mathrm{ms}^{-1}$, with the cases that indicate the best performance highlighted in green. More horizontal HFS angles improve drift-aided penetration, but face tighter engineering constraints on straight flight paths from a top-inboard injector. Deeper penetration at positive injection angles remained consistent in all simulations. However, while penetration depths for the higher temperature pedestals with the $\Delta_{\mathrm{DIII\text{-}D}}$ drift are encouraging (owing to a positive scaling with pedestal temperature), the cases excluding any drift effects and for the Δ_{HPI2} scaling exhibit the opposite dependence, favouring lower pedestal temperature. Thus, some additional care may be needed when selecting an optimum operating scenario in relation to pellet injection for fuelling.

Figure 7 indicates that negative injection angles need not be pursued further, owing to their poorer deposition performance, whereas positive-tilt solutions would present significant challenges in achieving the higher injection velocities required. The conclusion at this stage is therefore to retain the 0° injection line in the conceptual design phase.

The low aspect ratio ($A = 2.3$) of the device affords comparatively generous routing space for a pellet guiding tube, yielding favourable bend radii. As shown in figure 7, substantial deposition beyond the pedestal top ($\rho > 0.9$) is achievable even for modest launch speeds (300 $\mathrm{m\,s}^{-1}$ using the HPI2 scaling or 250 $\mathrm{m\,s}^{-1}$ for the DIII-D scaling). Nevertheless, pellet survivability in curved guide tubes is ultimately limited by centrifugal loading and surface erosion, which scale approximately as v^2/r. Experiments with 2–3 mm pellets have demonstrated transferable speeds of order $1\,\mathrm{km\,s}^{-1}$ for bend radii of ~ 6 m. An AUG-calibrated empirical relation for the maximum transferable velocity, adopted by Reiter *et al* [44], is given by

$$v_c\left(\mathrm{m\,s}^{-1}\right) = 1150\sqrt{\frac{r\,(\mathrm{m})}{\Phi\,(\mathrm{mm})}}, \tag{5}$$

where Φ is the pellet diameter. Applying this to the present 5 mm pellets shows that achieving $v_c \approx 1\,\mathrm{km\,s}^{-1}$ requires a minimum bend radius of only

$$r_{\mathrm{required}} \approx 3.8\ \mathrm{m},$$

well within the available geometric allowance of ~ 8 m between the magnetic axis and the vacuum vessel top in ST-E1. The operating envelope for the pellet injector therefore appears favourable, and coupled studies with transport simulations will be carried out in the next design stage to refine fuelling performance predictions.

3.2. Plasma exhaust

ST-E1's large vacuum vessel held at UHV (ultra-high vacuum) imposes stringent demands on pump performance, meaning that the tokamak's physical architecture must co-develop with credible, high-fidelity vacuum simulations. Although a detailed comparison of 18 versus 12-limb configurations is addressed in a companion publication [3], the present study uses the more challenging 18-limb case with an increased radial build and therefore a larger pumped volume, presenting more challenges for the exhaust system during both steady-state operations and the first pumpdown.

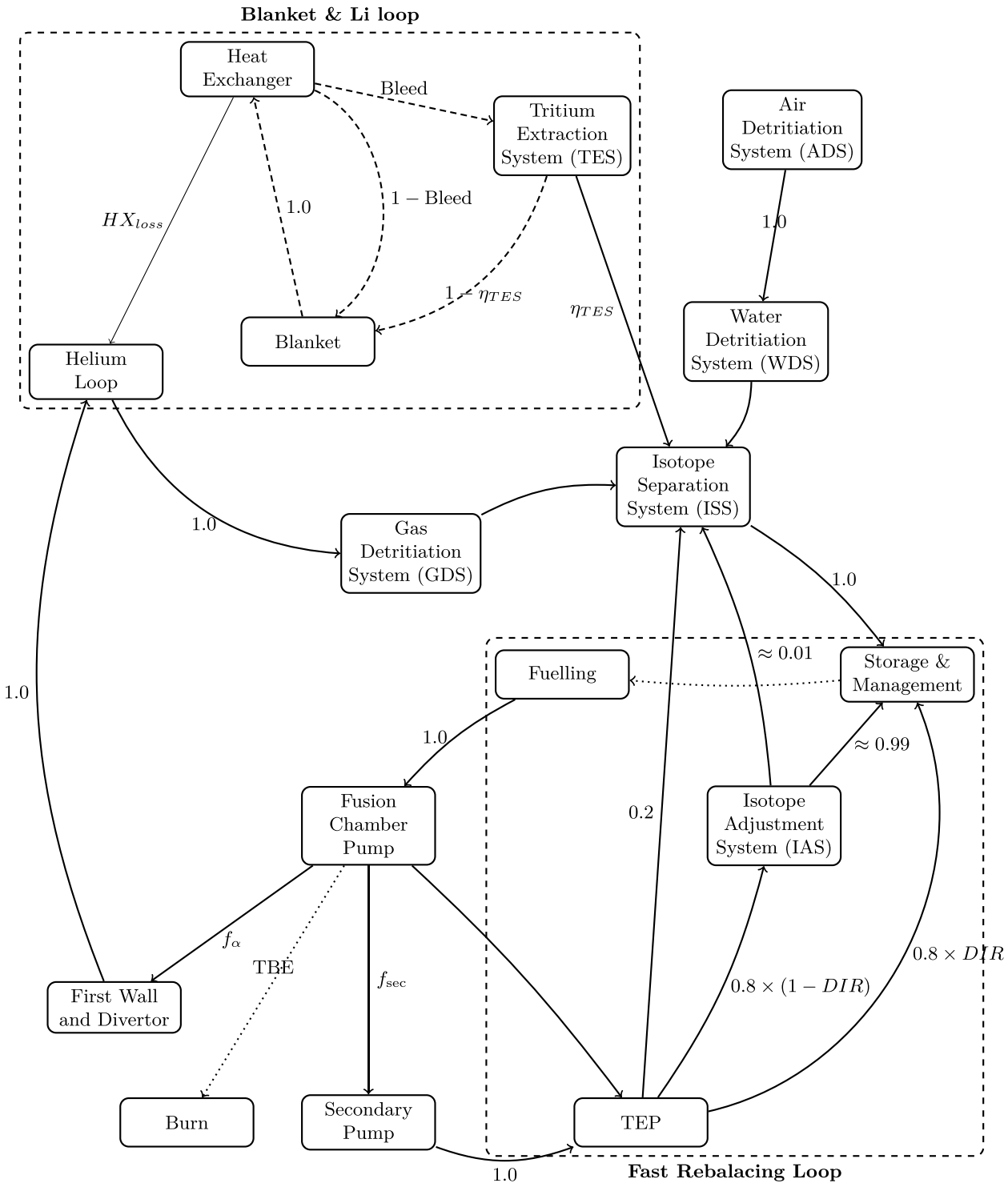

Figure 4. Integrated tritium processing plant for ST-E1, with flows labelled to match the PyFuel inventory model. Dashed lines represent lithium flows and the dotted line is the storage to fuelling line which is not simulated but rather a depleting and increasing source term for the storage and fuelling respectively of $\frac{\dot{N}}{\text{TBE}}$ is utilised. The stack and the retentate line from TEP (Tokamak Exhaust Processing) to GDS (Gas Detritiation System) are not shown for clarity of image.

While comprehensive studies on plasma edge behaviour and divertor pressure are set to be conducted concurrently [45], a preliminary evaluation of the vacuum duct geometry can be performed. The required conductance and pump speed, pending detailed SOLPS evaluations, assume an initial divertor pressure of 1 Pa. The conductance of the exhaust system pertinent to plasma operation and maintenance of the requisite divertor pressures were calculated using SPARTA [46], an

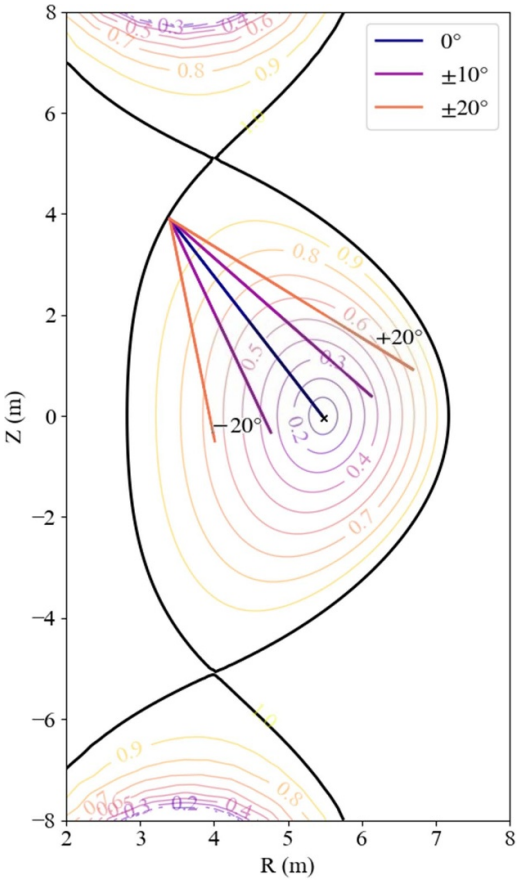

Figure 5. HFS injection lines. The trajectory that intersects the magnetic axis is the reference 0° line, and positive (negative) angles are in the anti-clockwise (clockwise) direction.

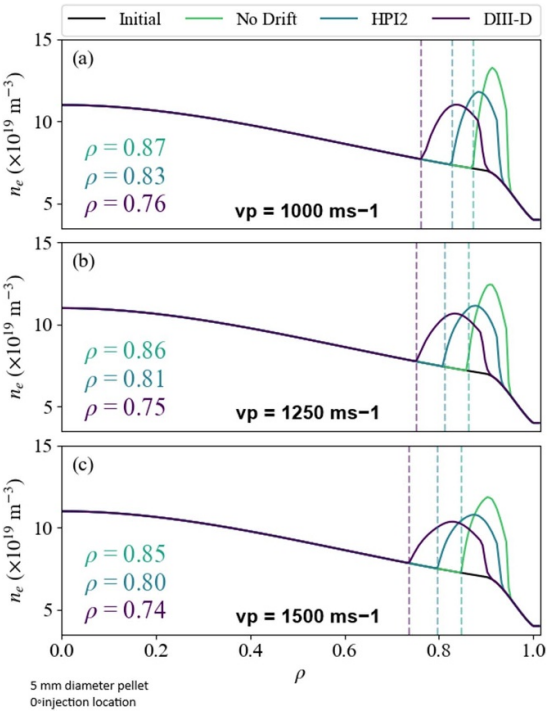

Figure 6. Preliminary pellet fuelling simulation result using a 5 mm diameter pellet at the 0° injection location for (*a*) $v_p = 1000$ ms^{-1}, (*b*) $v_p = 1250$ ms^{-1}, and (*c*) $v_p = 1500$ ms^{-1}. The black line is the initial density profile, and three deposition profiles are shown: without considering ∇B drift effects (light green); including the HPI2 drift scaling (teal); and including the DIII-D drift scaling (dark purple). The vertical dashed lines indicate the maximum penetration depth, with the corresponding ρ location given. The target for pellet penetration tends to be to penetrate further than the pedestal top.

open-source direct simulation Monte Carlo (DSMC) solver for rarefied gas flows.

The resulting pressure profiles from the analysis can be seen in figure 8 where the pressure at the divertor opening has been fixed to 1 Pa. The findings from the conductance analysis are illustrated in table 4, revealing a conductance value of 66 m^3 s^{-1} through the primary duct, supplemented by an additional 6 m^3 s^{-1} via the auxiliary dead zone port at a pressure of 1 Pa. The conductance was also analysed at lower pressure, giving an indication of the ports suitability for pumpdown as well as operating pressure maintenance. The conductance for different pressures can be seen in table 4. Figure 8 also indicates substantial flow accumulation in the region between the blanket and the shielding. This effect will be mitigated either by tailoring the geometry of the shielding volume located behind the blanket or by introducing additional conductance to the dead space, with the latter approach being carefully balanced against the shielding performance requirements.

The reference case P_{fus} and TBE$= 1\%$ can be taken to analyse whether this conductance is sufficient. By taking the gas temperature to be $T = 293.15$ K and ideal gas behaviour, the fuelling flow is:

$$\dot{n}_{\mathrm{in}} \approx \frac{\dot{n}_{\mathrm{burn}}}{0.01} \approx 9.26 \times 10^{-2}\ \mathrm{mol\,s^{-1}}. \tag{6}$$

The corresponding ideal-gas throughput is

$$Q = \dot{n}_{\mathrm{in}} R_c T \tag{7}$$

$$\approx \left(9.26 \times 10^{-2}\right) \times 8.314 \times 293.15 \approx 2.26 \times 10^{2} \quad \mathrm{Pa\,m^3\,s^{-1}}.$$

At $p_{\mathrm{div}} = 1$ Pa, the total pumping speed required is

$$S_{\mathrm{req,tot}} = \frac{Q}{p_{\mathrm{div}}} \approx 2.26 \times 10^{2}\ \mathrm{m^3\,s^{-1}}. \tag{8}$$

For N identical ports,

$$S_{\mathrm{req,port}} = \frac{S_{\mathrm{req,tot}}}{N}$$

$$\Rightarrow \begin{cases} N = 36: \ S_{\mathrm{req,port}} \approx 6.27\ \mathrm{m^3\,s^{-1}}, \\ N = 24: \ S_{\mathrm{req,port}} \approx 9.41\ \mathrm{m^3\,s^{-1}}. \end{cases}$$

The duct value $C_{\mathrm{eff}} = 72$ m^3 s^{-1} was obtained from flow simulations at this pressure and is therefore an *operating-point conductance*. In lieu of a detailed pump characteristic, we adopt representative inlet speeds for torus cryopumps and form a local linear estimate of the effective speed at the vessel plane:

$$S_{\mathrm{eff,port}} \simeq \left(\frac{1}{S_{\mathrm{pump}}} + \frac{1}{C_{\mathrm{eff}}}\right)^{-1}.$$

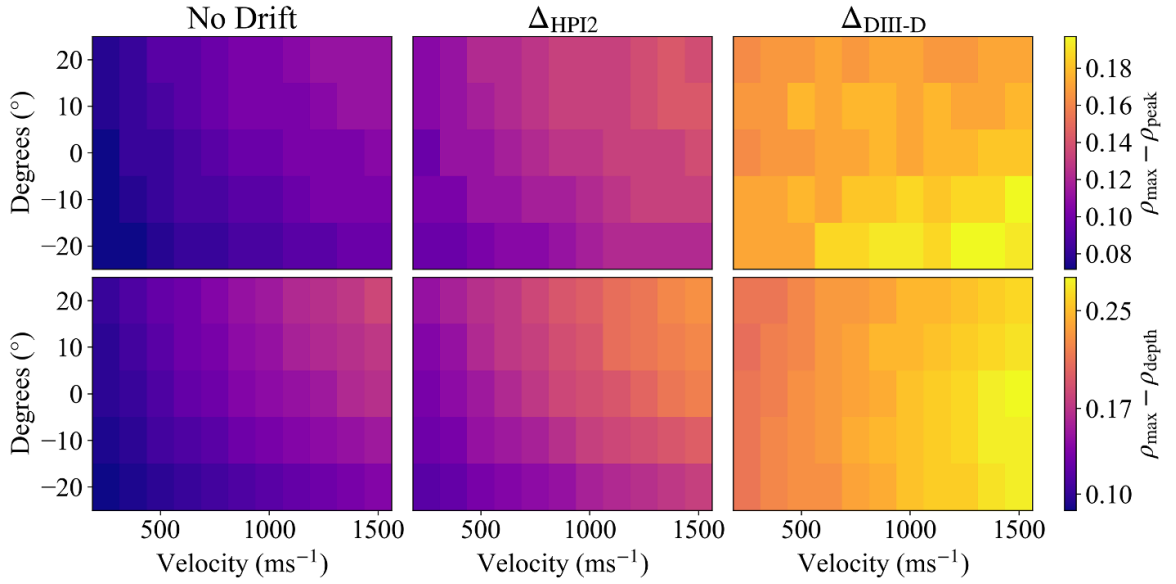

Figure 7. Total pellet penetration depth for varied velocities and angles, represented by $\rho_{\mathrm{max}} - \rho_{\mathrm{depth}}$ (top row), and $\rho_{\mathrm{max}} - \rho_{\mathrm{peak}}$ (bottom row), where ρ_{max} is the plasma edge + SOL width, ρ_{depth} the penetration depth (see dashed lines in figure 6), and ρ_{peak} the location of the density peak.

Pumping speeds can be taken from [47–49] and utilised in table 5. Even the conservative entries exceed the per-port requirement derived from mass balance ($\sim$ 6–9.5 m^3 s^{-1} for 36 vs 24 ports at $p_{\mathrm{div}} = 1$ Pa), indicating a comfortable margin at the present geometry.

3.3. Fast rebalancing and resupply

Tritium leaving the plasma exhaust vacuum system will be a mixture of hydrogenic species, Q, trace impurities, and helium ash. To enable the separation of Q from the remaining stream, a Pd diffuser set (usually Pd-Ag alloys to minimise hydrogen embrittlement [31]) will be utilised to provide a pure Q permeate stream and a trace T retentate stream. The current Pd diffusers for ST-E1 have been sized to provide 99.9% of the hydrogen isotopes to the isotope adjustment system (IAS) fast rebalancing loop as per the layout in figure 4[11]. While the cryopump vacuum systems may be able to do some initial separation [50, 51], these diffusers are considered the baseline to allow for full clean-up of the Q stream and are not affected by the close proximities of the Ne and T boiling point which would lead to cryo-based separation being a challenge. From there, an 80:20 split is taken, with 20 % going straight the main ISS, and 80%[12] going to the fast rebalancing loop.

As the pure Q stream enters the rebalancing loop there is a split where some species go straight to the fuelling system, referred to as the DIR fraction, and the other going to a dedicated IAS. This split is seen in figure 9. What limits the DIR fraction is the protium pickup. Sources of protium often include contamination in stainless steel components used throughout fuel cycle processing systems and (n,p) production in the fusion chamber during operation, both of which contribute to challenges in many fast-rebalancing systems.

Investigation of the operational limit for a cryogenic distillation-based IAS system for the purpose of protium removal was performed with the CryOgenic Distillation For Isotopic Separation of Hydrogen (CODFISH) code [52]. This code was developed at Savannah River National Laboratory (SRNL) to perform tritium inventory optimisation studies for continuously operated cryogenic distillation columns for hydrogen isotope separation. CODFISH estimates optimum steady-state column design and operating parameters using the bubble point method [53, 54]. The user constrains isotopic concentrations of the column outlet flows and they code estimates the CD (Cryo Distillation) column dimensions and operating conditions. The outputs of this model are the residence time in the column, system duty, and the isotope fractions present in the protium rich and return streams. For this work, the constraint on the IAS system was to deliver a combined fuelling return stream with less than 0.8 at% protium while achieving a T/D ratio $>$1.0. Each theoretical stage was assumed to be 5 cm, with a maximum of 70 stages. The total height of the column is therefore limited to 3.5 m, which is considered a maximum to fit in a reasonably sized glovebox. To determine the optimal column geometry for the given constraint, CODFISH sweeps over column configurations and determines the minimal number of theoretical stages

[11] A key parameter requiring further design elaboration is the pressure differential between the divertor exhaust ($\approx$1, Pa) and the operating pressure required for the PdAg diffuser. An all-metal vacuum pumping chain—likely comprising a turbo-molecular pump followed by a bellows or roots compressor—would be required to bridge this gap whilst maintaining tritium compatibility. The residence time and inventory implications of this compression stage are left for detailed process design.

[12] The IAS is sized for $\approx$ 100% flow, but for a more conservative estimate and operational flexibility 20% is sent to the main ISS.

Table 3. $\rho_{\max} - \rho_{\text{depth}}$ for $v_p = 1000\ \text{ms}^{-1}$ and $d = 5.0$ mm (straight guiding tube). Maximum penetration depth in each parameter set is highlighted in green.

p_{ped} (kPa)	T_{ped} (keV)	n_{ped}	w_{ped} (psiN)	$f_{\text{GW, ped}}$	Case	-20°	-10°	0°	10°
133	6.8	6.16	0.081	0.60	No drift	0.0766	0.0816	0.0867	0.0917
					Δ_{HPI2}	0.1368	0.1519	0.1619	0.1720
					$\Delta_{\text{DIII-D}}$	0.2974	0.3024	0.3024	0.3024
106	4.7	7.05	0.074	0.75	No drift	0.0816	0.0917	0.0967	0.1017
					Δ_{HPI2}	0.1419	0.1619	0.1720	0.1820
					$\Delta_{\text{DIII-D}}$	0.2523	0.2573	0.2623	0.2623
102	3.5	9.07	0.085	1.00	No drift	0.0967	0.1067	0.1168	0.1218
					Δ_{HPI2}	0.1569	0.1770	0.1920	0.2021
					$\Delta_{\text{DIII-D}}$	0.2422	0.2472	0.2572	0.2573
139	6.1	7.14	0.090	0.75	No drift	0.0816	0.0867	0.0917	0.0967
					Δ_{HPI2}	0.1419	0.1569	0.1669	0.1770
					$\Delta_{\text{DIII-D}}$	0.2623	0.2673	0.2673	0.2723

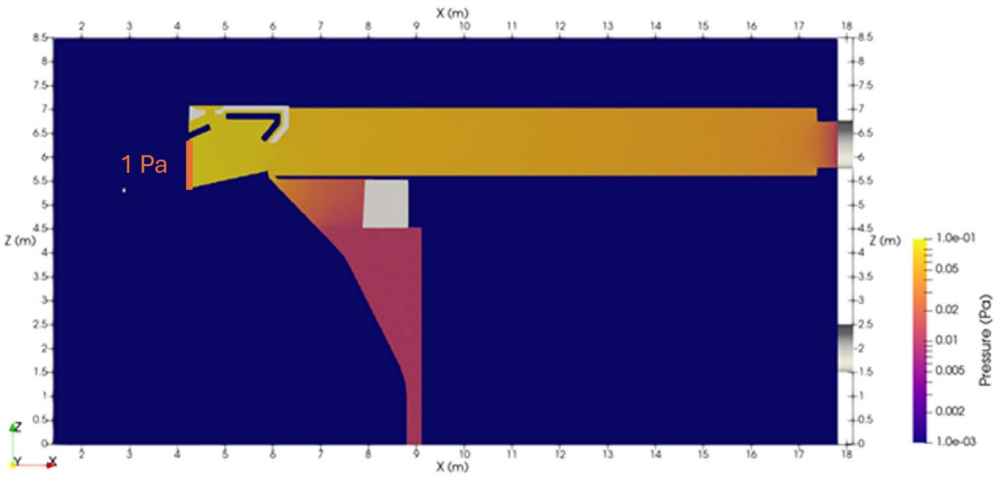

Figure 8. Pressure profile of the vacuum duct for a operating point pressure of 1 Pa calculated with direct simulation Monte Carlo analysis in SPARTA.

Table 4. Flow properties and results for three inlet pressures.

	$P_{in} = 1$ Pa	$P_{in} = 0.1$ Pa	$P_{in} = 0.01$ Pa
T_{in}	300 K	300 K	300 K
Total *M*flow	72 Pa m^3 s^{-1}	3.85 Pa m^3 s^{-1}	0.3 Pa m^3 s^{-1}
Conductance	72 m^3 s^{-1}	38.5 m^3 s^{-1}	30 m^3 s^{-1}
Duct	66 m^3 s^{-1}	37.65 m^3 s^{-1}	28.85 m^3 s^{-1}
DeadSpace	6 m^3 s^{-1}	0.85 m^3 s^{-1}	1.15 m^3 s^{-1}

Table 5. Per-species inlet speeds and effective per-port speed at $C = 72$ m^3 s^{-1}.

Gas	S_{pump} (m^{3}s^{-1})	$S_{eff,port} = \frac{S_{pump}C}{S_{pump}+C}$ (m^3 s^{-1})
D_2	55	31.2
DT	49	29.2
He	52	30.2
H_2	78	37.4

required to achieve the given input constraint. For each column configuration, steady-state flow profiles, temperature profiles, column height and diameter, reflux ratio, system duty, and steady-state tritium inventories are calculated.

The results in figure 10 show the final protium percentage for different initial protium concentrations, in addition to the number of theoretical stages required. From these figures, it is clear that there is a trade-off. Going to a higher DIR fraction increases the final protium inventory but reduces the inventory and mass flow in the IAS. Comparatively, lower DIR fractions lead to lower residence times in the IAS, as bulk processing of more mass flow means the number of stages are normally reduced to achieve the same protium requirement, and the increased flow rate further improves the separation efficiency of the column. It can be seen that while there may be some benefit in increasing DIR fraction, many of these fall outside of the required protium target. It also shows that minimal stages are required for the lower DIR fractions, with even 50% DIR only requiring 12 stages for an inlet of 1 at% protium.

Figure 11 presents the isolines corresponding to the fuelling stream protium concentration of 0.8 at.%. These isolines are expressed as a function of the scaled residence time relative to the DIR fraction calculated as:

$$\tau_{pr} \times (1 - f_{DIR})$$

where τ_{pr} is the residence time in the protium removal column and f_{DIR} is the DIR fraction. This is effectively the average residence time in both the protium removal stream (from CODFISH) and the stream that goes directly to fuelling (assumed negligible), thus this is the effective residence time of the total rebalancing loop.

Figure 11 also shows that even for the higher protium inlets the residence time of the IAS can be low as long as the DIR fraction is low. This is due to the residence time in the protium removal column being low (only coarse separation is required at low DIR fraction to the large flow) meaning the residence time of this system is still < 150 s. The results also show that increasing the DIR fraction increases the overall residence time of the IAS for the 1.5 and 2.0 at% inlets. This would negatively affect the overall steady-state tritium inventory of the system contrary to common understanding. The only system

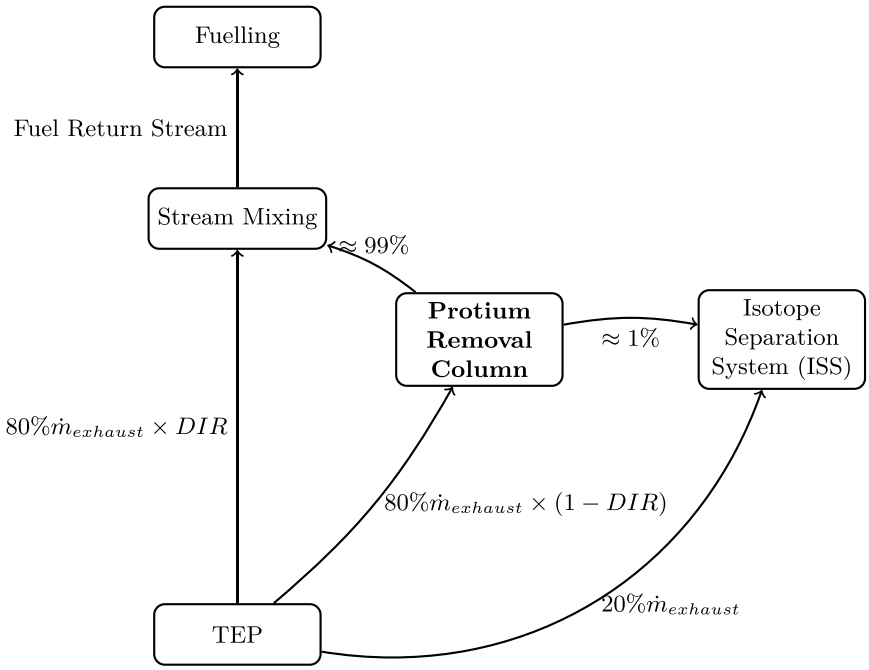

Figure 9. Set-up for the CODFISH runs for the ST-E1 reference design point with a TBE of 1% to size a protium removal column as the isotope adjustment system. Note the 99% return fraction is the tritium only return, not the total mass flow return.

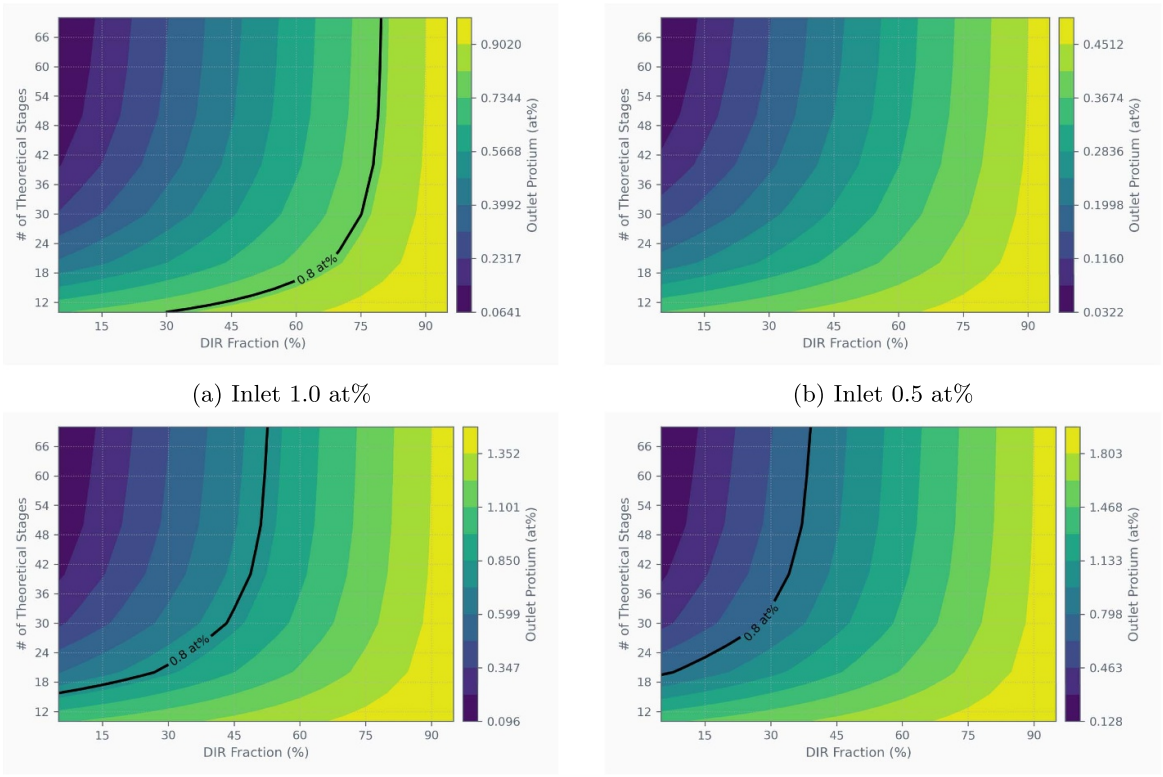

(a) Inlet 1.0 at% (b) Inlet 0.5 at%

(c) Inlet 1.5 at% (d) Inlet 2.0 at%

Figure 10. Outlet protium (at%) contour maps versus DIR fraction and theoretical stages for four inlet compositions. The bold line marks the 0.8 at% specification.

that shows any benefit with higher DIR fractions is if the protium inlet concentration is low, as the system will be able to send more directly to the fuelling system.

Overall, what these results show is that a sensibly sized, $<$ 3.5 m, CD column can manage inlet protium concentrations ranging from 0.5 to 2.0 at% enabling fast resupply of 80% of

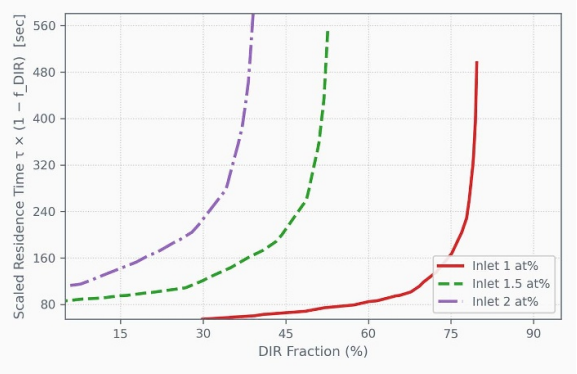

Figure 11. Figure detailing the 0.8 at% isoline for the different atomic inlet percentages. Note that 0.5% inlet meets the criteria at all DIR fractions and therefore the isoline does not feature on this plot.

the outlet stream from the TEP, with a low overall residence time and inventory of the IAS system. This will reduce the steady state inventory of ST-E1's tritium plant and may lead to a reduction in the required startup inventory.

3.4. Tritium loss

Tritium loss in the plasma facing components (PFCs), along with losses previously ascribed in the heat exchanger, is a significant source of tritium loss in the fuel cycle. These components are most affected by the plasma and operating conditions and PFCs form key pathways for tritium permeation into the helium coolant. To relate the losses in the PFCs to wider tritium behaviour in ST-E1 the PFCs can be divided into three sections: the divertor, centre column first wall, and breeder blanket first wall. Although all components have the same material systems, their experienced operating conditions are different, which affects their thickness profiles to satisfy the flux and structural requirements. In this study, the Tritium Migration Analysis Program, Version 8 (TMAP8) was utilised, in addition to its surrogate model features to develop this first assessment [55].

To prioritize rapid iterations, one-dimensional (1D) simulation geometries were considered to allow this to quickly deliver simulation results and adapt to evolving design decisions. The decision to use a 1D geometry with a simplified tritium model using a single trapping site when TMAP8 is able to perform more complex analysis [56] was motivated by the short term goals of this effort: enable (1) rapid design space exploration, (2) surrogate model development, and (3) multiscale analysis from the component scale to the fuel cycle. These aims are facilitated by prioritise a fast-running model with fewer parameters to quickly get modelling data. The model formulation and parameters are nonetheless informed by literature data to ensure accuracy, but we recognize that a more sophisticated geometry (e.g. 2D, 3D) and model (e.g. irradiation effects, more diverse trapping sites) would provide higher fidelity and potentially quantitatively affect the analysis performed here. This expansion to higher-fidelity modelling

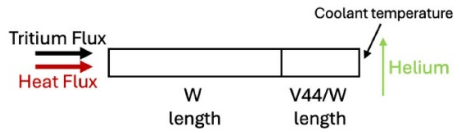

(a) Schematic configuration for PFCs, which includes a tungsten armour and a V44 or tungsten pipe. Tritium and heat fluxes inject the plasma surface in tungsten armour, helium flow removes the released tritium and heat from the coolant surface.

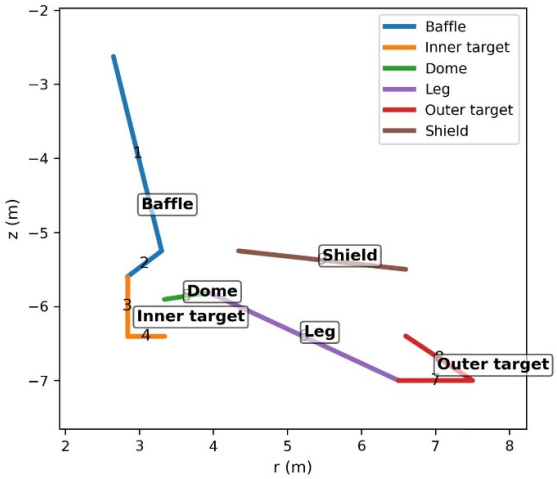

(b) 2-D divertor schematic utilised for analysis of possible tritium flux into the coolant and residence time with the plasma facing components.

Figure 12. (*a*) 1-D divertor schematic used for tritium transport analysis (*b*) plasma-facing component with the different regions, in 2D.

is left for future, more refined design studies when accuracy needs warrant higher computational costs. A more extensive discussion is available in [57].

The tritium behaviour includes implantation, diffusivity, solubilities, surface reactions, and a simple description of trapping behaviour with one trapping site, utilising data from [18]. The general schematic structure of these PFCs in 1D is shown in figure 12(*a*). The surrogate model was developed with the parameters seen in supplementary information A.4 for a data set of 3200 simulations, with a precision of the residence time prediction of 17.93% and of the ratio of the impinging flux to the permeated flux (termed α) of 10.88% . The surrogate was then used in combination with a simplified divertor geometry to examine a worse case for tritium permeation flux into the coolant and the effective residence time of said permeation for total particle impingement on the divertor. The divertor schematic can be seen in figure 12(*b*). Further details of this study are the focus of a publication in preparation [57], with a brief summary in supplementary information A.4. The residence time is calculated by fitting the time-dependent tritium

flux at the coolant surface J_{back} using the following exponential form:

$$J_{\text{back}} = J_{\infty}\left(1 - \exp\left(-\frac{t}{\tau}\right)\right), \tag{9}$$

where J_{∞} is the steady-state tritium flux at the coolant surface, t is the time, and τ is the residence time. The calculation of this residence time and the development of a new two-parameter residence-time model, which more accurately captures delayed tritium release from PFCs, are presented and compared in Yang *et al* [57].

The results give an indication of the total tritium retained in the PFCs and in the helium coolant. A value of 8 mm for the W armour thickness and 1 mm for the V44, with a helium coolant set at 400 °C, was selected for a subset, batch A, and a full tungsten, 8 mm thick, with a 600 °C coolant, batch B, was selected to represent the divertor options in [45] . The area of the divertor was taken from [45]. The heat flux and particle flux distributions were then varied across each region of the divertor, with the upper bound of the heat flux having to sum to a $P_{\text{SOL}} = 300$ MW and a particle flux summing to 9×10^{-2} mol s^{-1} total across the divertor surface area. 1000 scenarios were then generated with varying heat and particle fluxes to meet these constraints. Figure 13 details the distributions of these scenarios. The α values for both batches remain similar, as the higher temperature of batch B is offset by the higher diffusivity of batch A. Both systems show relatively low permeation loss, but the system with the vanadium alloy included, batch A, shows an increased residence time consistent with the higher solubility in the material, with the residence time being an order of magnitude higher which would cause an increased tritium inventory.

The preliminary evaluation excluded key phenomena, such as the dynamics at the interfaces at W and V44, from any compositionally complex layers that may form, or surface recombination kinetics in the coolant [58]. In addition, conservative estimates of the flux of tritium (total injected tritium deposition in the divertor region) give an upper bound limit of losses to the coolant and residence time. Such behaviours may mitigate some of the flux transferred to the coolant, but may also result in higher retained tritium in the components, being detrimental to the mechanical properties and retained tritium inventory in the components. This analysis will be the building block as further PFC and overall design development continue, with these surrogates directly interfacing with the inventory models described in section 4.

3.5. Tritium safety

The tritium safety basis for ST-E1 follows the DOE fusion facility framework, with *confinement* as the primary public-safety function. In line with DOE-STD-6002-96 [59], the plant is designed to keep tritium and tritiated compounds within engineered barriers and ventilated, filtered volumes, applying defence-in-depth, ALARA, and clearly defined technical safety requirements (TSRs).

Day-to-day design and operation adopt the capture-contain-cleanup philosophy of DOE-STD-1129-2015 [60]: tritium-handling equipment is located in ventilated, abated areas; process systems are backed by gloveboxes or secondary confinement; and dedicated monitoring is provided (tritium air monitors on workspaces and exhaust, stack/duct monitors, and O_2 monitors for inerted enclosures). Practical measures include fire barriers and fire protection compatible with tritium contamination control, engineered liquid handling to avoid uncontrolled flashing, strict control of oxidants in hydrogen-isotope systems, and provision for remote indication and testing of credited monitors.

At the analysis level, the tritium design is embedded in a graded Documented Safety Analysis following DOE-STD-3009-2014 [61], which identifies hazards, evaluates unmitigated and mitigated releases, and allocates safety-class and safety-significant controls (including confinement, ventilation alignments, monitoring, and fire protection). Tritium material control and accountancy (MC&A) follow DOE O 474.2A and DOE-STD-1194-2019 [62, 63], using material balance areas, key measurement points, calibrated measurements, and regular physical inventories. Collectively, these standards provide a structured starting point for the ST-E1 tritium safety design basis and its integration with the blanket and fuel cycle.

4. Tritium plant modelling

The tritium plant can be scoped using inventory models such as those of Abdou *et al* [38] and Meschini *et al* [64]. For this, PyFuel (a Tokamak Energy code benchmarked vs RHINO from Savannah River National Laboratory [65]) has been used to understand the overall tritium plant behaviour.

This model builds upon typical inventory models by including the work and discussions demonstrated in this paper in prior sections to give either more realistic, or ST-E1 specific, values to the input parameters. These include work from section 2:

- The use of a baseline TBR of 1.113 as per the range $1.085 \leqslant \text{TBR} \leqslant 1.14$ for the reference case
- Incorporation of a dynamic tritium extraction efficiency, seen in figure 14, to account for the challenge of tritium extraction from lithium
- The loss fraction for the heat exchanger as derived at the highest operating temperature for V44, $\text{HX}_{\text{loss}} = 1.4 \times 10^{-3}$

In addition to the work from section 3:

- TBE of 2% for the reference case, which accounts for the positive fuelling characteristics seen in the pellet fuelling simulations
- CODFISH results were utilised to determine the processing time of the IAS system depending on the protium inlet concentration
- PFC input taken from upper bound values from the surrogate models, with the residence time $\approx$ 24 h and loss fraction into the coolant of 10^{-3} to cover the majority of the τ and α parameters for both cases

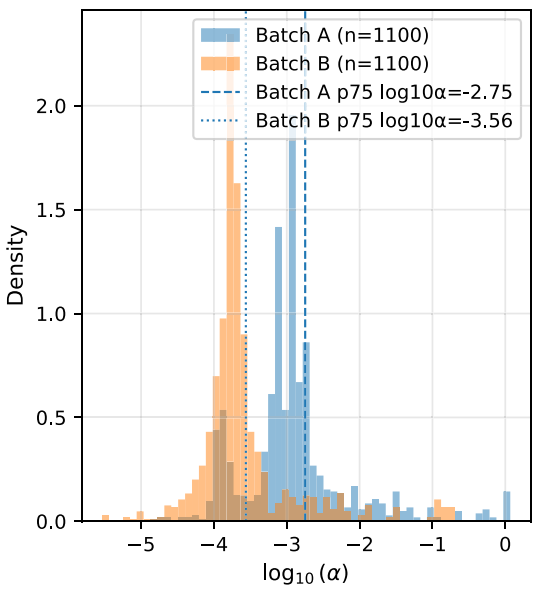

(a) Overlayed density histograms of $\log_{10}\alpha$ for Batch A and Batch B. Vertical dashed lines indicate the 75th percentile (p_{75}) of each distribution.

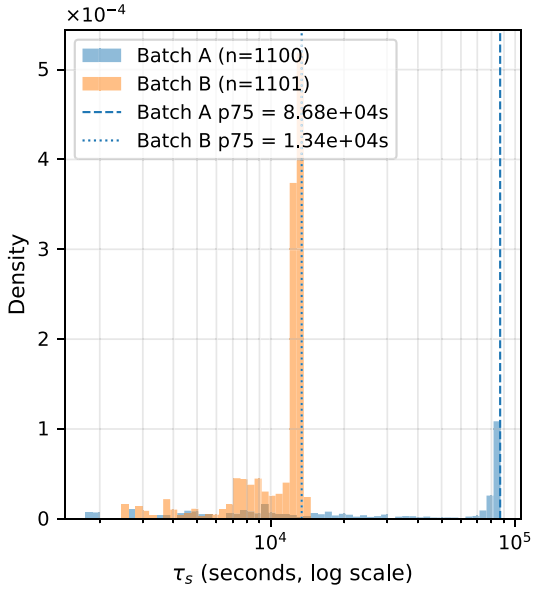

(b) Overlayed density histograms of residence time τ_s for Batch A and Batch B. Vertical dashed lines indicate the 75th percentile (p_{75}) of each distribution.

Figure 13. Comparison of flux ratio α and residence time τ_s distributions for the two surrogate batches. Histograms are normalised to probability density to allow direct comparison between batches with different sample counts. Batch A corresponds to the lower-temperature case (673 K), while Batch B corresponds to the higher-temperature, W-only case (873 K).

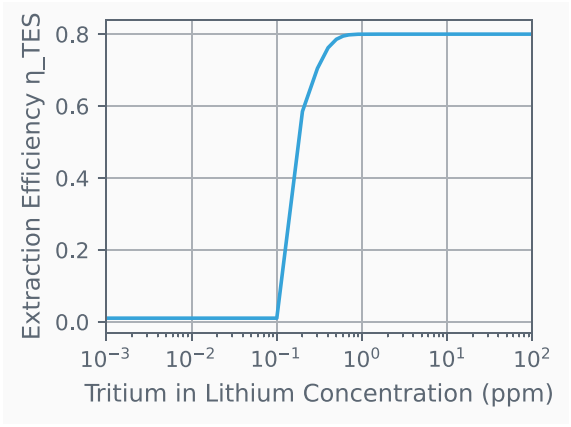

Figure 14. Concentration dependent extraction efficiency for the TES system, built into PyFuel.

Together, these feed the reference design case for ST-E1's fuel cycle modelling, which further serves as the baseline for sensitivity studies. Such a baseline will be updated as the design develops, where critical factors such as irradiation induced blanket retention can be elucidated from the complex mass transfer behaviours of tritium in MHD-influenced lithium flow [66, 67] as a key example. This therefore means some parameters may be optimistic, despite margin being built in.

4.1. Reference design case

The reference design case for ST-E1 can be simulated to assess the start-up and steady-state inventories of the plant, which are key to the initial viability of the system and the maximum allowable tritium inventory in a component taken to be 100 g to prevent off-site evacuation. The overall parameter set for the reference design case can be seen in tables supplementary A.1. The reference design scenario for this plant posits a TBE of 2%, thereby presupposing $\eta_{\text{fuel}} = 76\%, f_{\text{burn}} = 2.6\%$ for an R of 0.1, or $\eta_{\text{fuel}} = 68\%, f_{\text{burn}} = 2.9\%$ for an R of 0.2[13]. A DIR fraction of 0.7, with a protium inlet concentration of 1 at% and an outlet concentration of 0.8 at.% was taken. The remaining input parameters, including flow fractions and residence times, are presented in the supplementary A.1 of this paper, with their values obtained from the available literature where possible [31, 38, 64, 68]. Figure 15 details the time evolution of the inventories of each component simulated.

The reference case produces a startup inventory of 1.58 kg, which includes a 20% contingency budget for commissioning (1.31 kg for a tritium lean system). Furthermore, the requirement for self-sufficiency is well met, with a doubling time

[13] More details in the supplementary A.2 on the relationship of R to TBE.

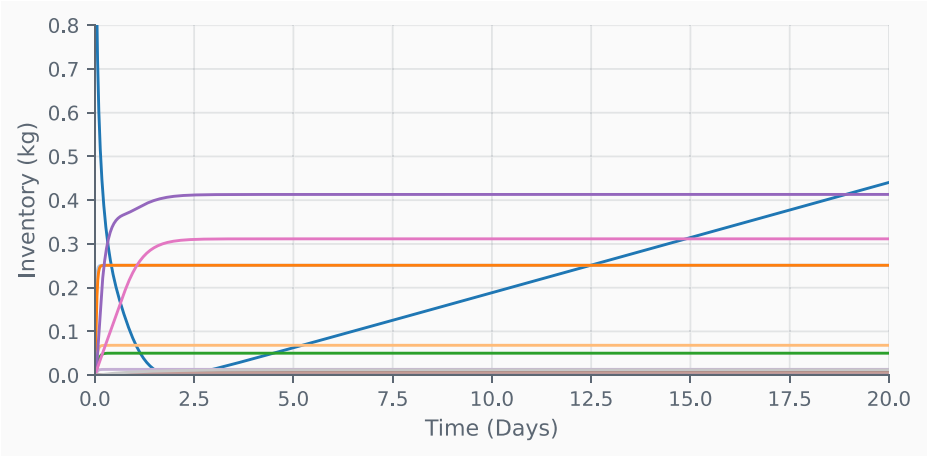

(a) Component inventories over the first 20 days.

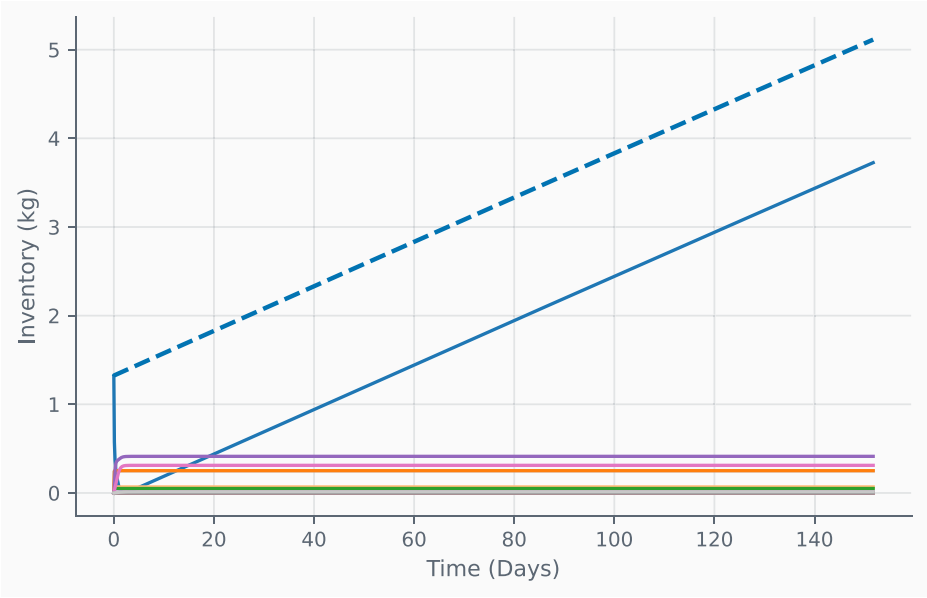

(b) Component inventories over the full simulation period.

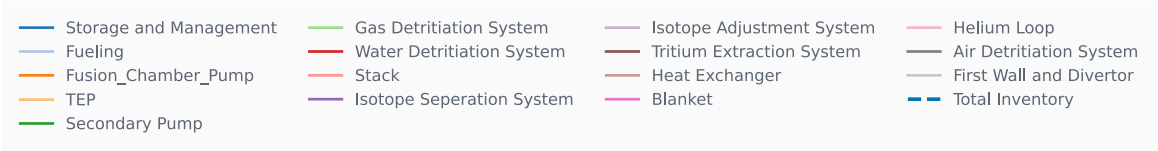

Figure 15. Inventories of all tritium plant components: (*a*) zoomed view of the first 20 d; (*b*) full time-series. Simulated for tritium lean system (i.e. no contingency in startup inventory).

coming out to 152 d.[14] It should be noted that the availability of the simulation is assumed to be 100% Current simulations on availability do not dynamically capture relevant plant behaviour, with much of the gold standard centring around a total tritium plant off time dictating a given reserve inventory required as in [38]. In a real tritium plant, it is highly unlikely that the entire plant will be shut off in such a way; therefore, a 20% contingency was assumed. A time to an *operational inventory* as in [65] was also included, with the time to I_{op} for the reference case being 85 d and a required value of 2.4 kg. This is calculated through:

$$I_{\mathrm{op}} = \frac{\bar{N}}{\eta_f f_b} t_r \left(1 - f_{\mathrm{TEP}\to\mathrm{IAS}}\right). \tag{10}$$

With a reserve time, t_r, being 24 h. This is effectively the amount of time the system would be required to operate with just the fraction of the flow from the TEP to the IAS, $f_{\mathrm{TEP}\to\mathrm{IAS}}$, and therefore gives the amount required to cover the remaining tritium mass. The build-up of tritium in the storage system, with the time to operational inventory and doubling time marked, can be seen in figure 16.

[14] The doubling time is defined as in Malone *et al* [65] detailing the use of I_{op} as described latterly.

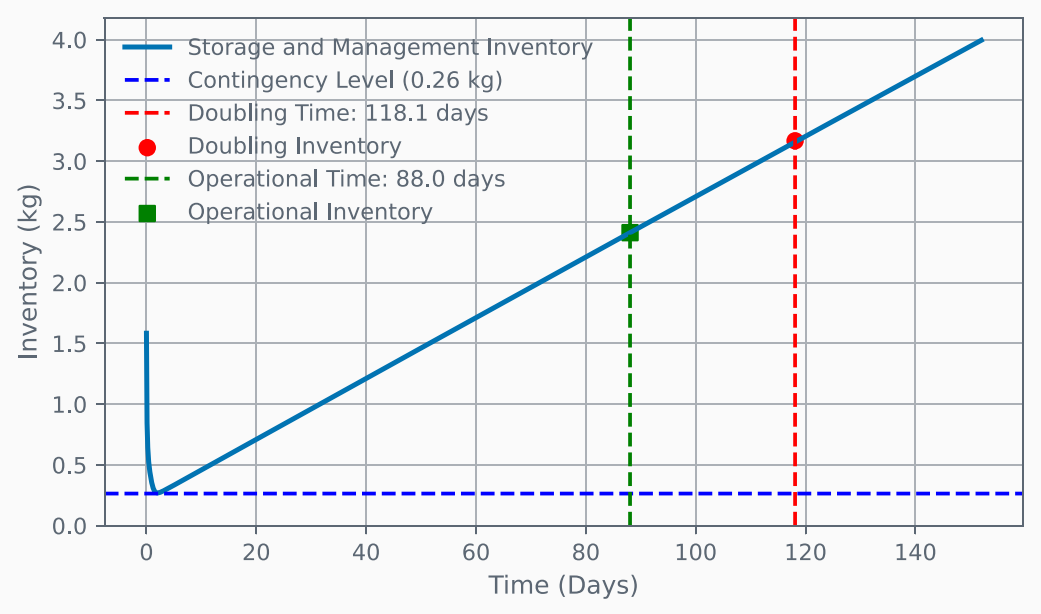

Figure 16. Figure detailing the tritium inventory build up in the storage system for the reference design case. The time to I_{op} and $I_{double} = 2 * I_{start}$ (classic doubling time) are marked, with the total run being to the doubling time set out in the text of $I_{double} = I_{op} + I_{start} * (1 + contingency)$ of 152 days.

The final inventories, dependent upon TBE, can be seen for each component in table 6. This highlights key components that may require modularisation to reduce the inventory involved in any accident scenario. The blanket, fuelling system, chamber pumps, and isotope separation systems sit above the 100 g threshold. For the blanket system, the lithium loops are already split per segment, reducing the tritium hold up in each component, while the remaining systems are likely to either already be or can be made modular. Multiple pellet injector systems will be required for redundancy within the fuelling system and cryopumps are additionally proposed to be per segment. The main ISS has relatively little detail at this stage, but these initial simulations push the system to a modular configuration, either of a set of cryo distillation columns or, potentially, the modularisation may allow for the use of TCAP [69].

Together, these results indicate that the reference architecture and blanket choice can satisfy self-sufficiency with credible margin. The startup inventory of 1.6 kg, though, is not an insignificant amount of tritium; therefore, exploration of routes to reduce it and the sensitivity of that value to key dynamics must be explored. The following section looks at the effect of various parameters on the startup inventory, with this being simulated without a 20% contingency.

4.2. Key sensitivities

Further development of key systems will aid confidence in the reference design case; to that end, key sensitivities must be ascribed to select systems to help foster the correct technology development in concept design. Four key factors for ST-E1 that drive the overall startup inventory can be explored:

- Tritium breeding ratio
- Fuelling efficiency and burn fraction
- DIR fraction
- Lithium blanket inventory

4.2.1. TBR. The evolution of the TBR from the earlier design has indicated a reference TBR range of 1.085–1.14. While TBR has minimal impact on the startup inventory, it has a strong correlation with the doubling time of the plant. ST-E1, in its pilot phase, has no doubling time mission but seeks to cover inventory loss through either decay or system dynamics, thus reducing the burden on the required TBR. Despite this, the TBR has been assessed to understand the doubling time and the margin the system has. The large jump from a TBR of 1.10 down to 1.05 in figure 17 implies the system is approaching the TBR_{req} for self sufficiency. At these low TBRs, the required TBR becomes more sensitive to availabilities due to the loss term from decay becoming more important. For this reason, the target TBR of 1.10 for ST-E1 is maintained in order to avoid straying into regions where this may become a significant issue.

4.2.2. Fuelling efficiency and burn fraction. Although the burn fraction will arrive later from deeper physics simulation and, more importantly, commissioning and experimentation on ST-E1 itself, the fuelling efficiency has been explored. Figure 18 shows the variation of startup inventory with fuelling efficiency and how the recycling coefficient will affect the start-up due to its relationship to burn fraction. While a key parameter, the larger influence is from the fuelling efficiency due to the limited range of burn fractions between recycling coefficient $0.0 \leqslant R \leqslant 0.4$, with these being a sensible range of

Table 6. Final tritium inventory by subsystem after a full doubling time (with 20% contingency) (kg) to two significant figures.

Subsystem	Inventory (TBE = 2%) (kg)	Inventory (TBE = 1%) (kg)
Fuelling	0.25	0.50
Fusion Chamber Pump	0.25	0.50
TEP	0.07	0.14
Secondary Pump	0.05	0.10
Gas Detritiation System	0.0025	0.0045
Water Detritiation System	0.0035	0.0070
Stack	2.7×10^{-5}	6.1×10^{-5}
Isotope Separation System	0.41	0.79
Isotope Adjustment System	0.013	0.027
Tritium Extraction System	0.0061	0.0061
Heat Exchanger	0.0048	0.0048
Blanket	0.31	0.31
Helium Loop	2.1×10^{-4}	3.5×10^{-4}
Air Detritiation System	7.4×10^{-5}	1.5×10^{-4}
First Wall and Divertor	0.012	0.024
Total (excl. storage)	1.39	2.42

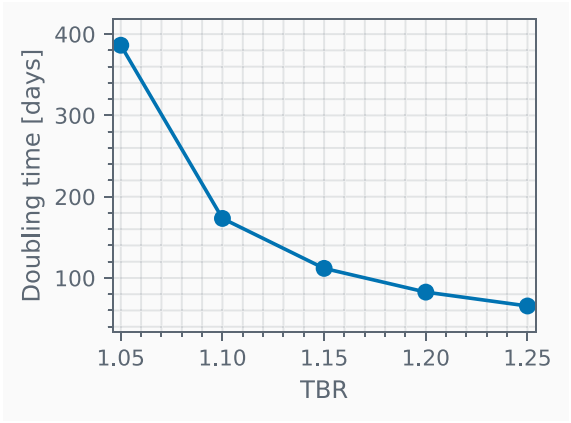

Figure 17. Figure detailing the variation of doubling time for different TBR values.

R for such a high power device. Remaining below 2 kg startup inventory is shown to require fuelling efficiencies of $\geqslant$50%.

Initial pellet simulations indicate that pellets of sufficiently large size (diameter $\geqslant$5 mm) and injection velocities exceeding 300 m s^{-1} tend to penetrate into the pedestal region, as illustrated in figure 7. These favourable results suggest that high fuelling efficiencies are achievable in ST-E1, which is essential if the recycling coefficient is low, as is anticipated for power-plant-scale devices.

Figure 18 demonstrates the pronounced influence of fuelling efficiency on the required startup tritium inventory, with this parameter dominating over the effect of the recycling coefficient. This behaviour has been extensively analysed in previous studies, such as Meschini *et al* [64], thereby underscoring the importance of the favourable high-field-side fuelling characteristics of ST-E1.

The substantial uncertainties associated with both recycling coefficients and fuelling performance in power-plant-relevant devices imply that achieving and characterising high fuelling efficiencies must remain a central design objective and be developed in parallel with the device design process. Consequently, the pilot phase of ST-E1 will be crucial for establishing the baseline of this key aspect and for quantitatively constraining this critical parameter.

4.2.3. DIR fraction. The CODFISH results were implemented in the PyFuel inventory model to explore the effect of input concentration on the startup inventory for different DIR fractions. For each DIR fraction, the required number of stages for the CD column, and therefore the residence time of the IAS, was calculated from interpolation tables of the CODFISH results. The inlet protium concentration was also scanned to understand the effect of protium pickup prior to this system.

Figure 19 shows the results obtained for different concentrations of protium inlet. What can be seen is a *jump* at the same points as the isoline levels from figure 11 for each of the different protium percentages of 1.0, 1.5, and 2.0 at.%. Any results after those values are where the column fails to reach the required outlet protium percentage and are shown as open symbols. This also shows the relative insensitivity of the startup inventory to the DIR fraction with only inlet protium percentage of 1 at% showing a positive trend with increasing DIR fraction. This is due to the flow split in figure 9 and its relationship to the processing time. While a higher DIR fraction allows for more to be directly reinjected into the fuelling system, the flow going to the CD column must be processed for a longer time, thus nullifying the benefit of the increased flow directly to the fuelling system. These are contrary to results often reported for increasing DIR fraction, where a near-linear reduction in startup inventory is often reported with increasing DIR fraction [64, 70], which being presented as a positive trend. This work here has shown this trend to not always hold true, and increasing DIR fraction can have a negative effect on the startup inventory. In addition, the increase caused by a higher protium inlet percentage is seen to be minimal, with the total range of startup inventories varying between 1.31 and

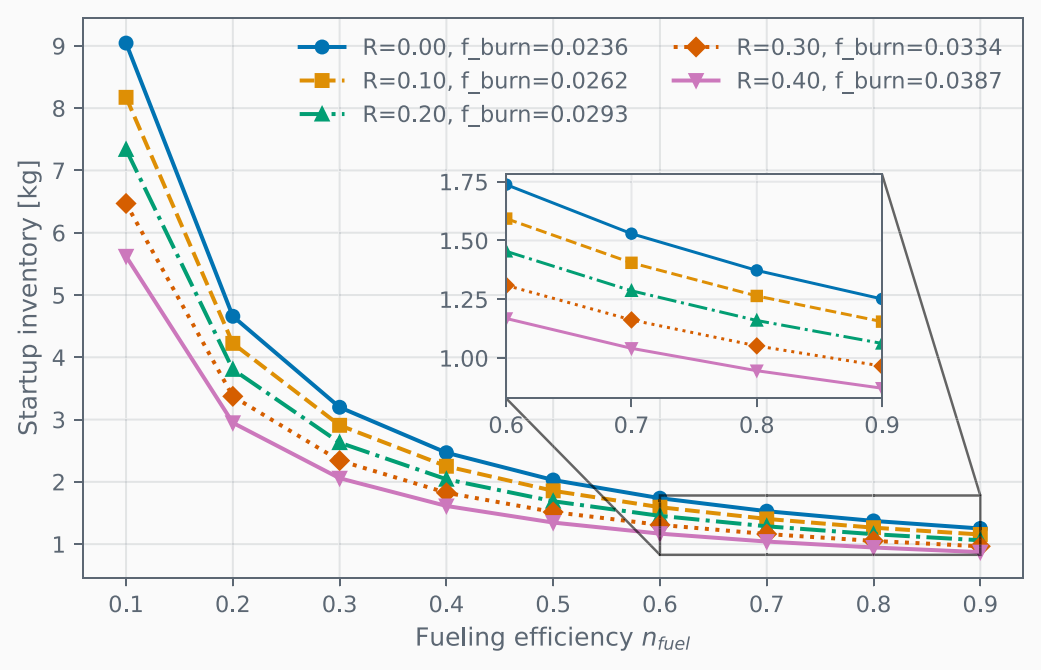

Figure 18. Tritium self-sufficiency sensitivity looking at the impact of fuelling efficiency for different recycling coefficients and therefore burn fractions.

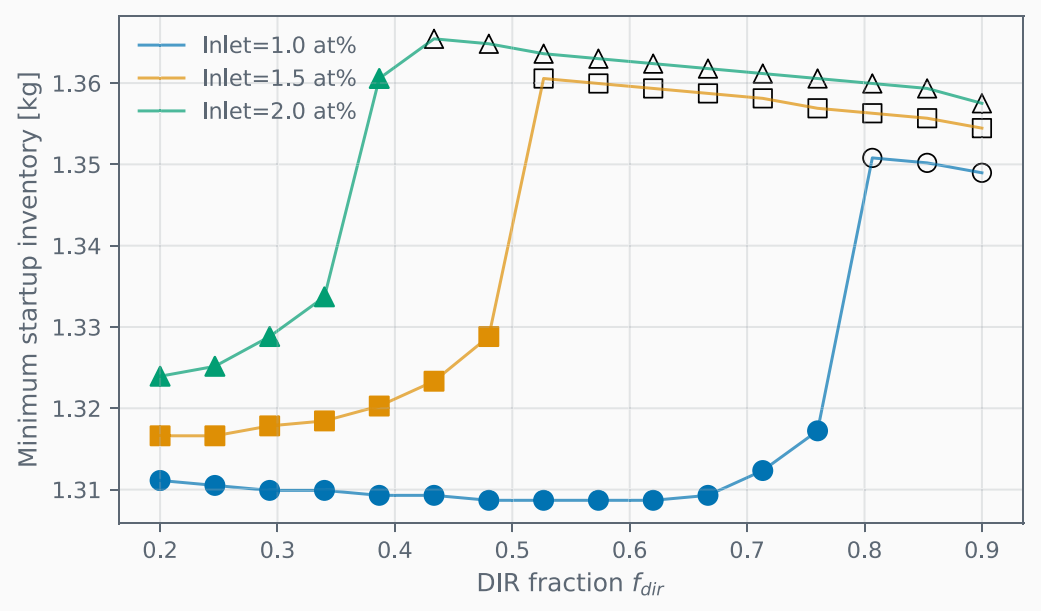

Figure 19. Minimum tritium startup inventory as a function of the direct internal recycling (DIR) fraction for three inlet protium concentrations (1.0, 1.5, and 2.0 at%). Filled markers indicate cases in which the isotope adjustment system (IAS) meets the outlet protium specification of 0.8 at%, while hollow markers denote cases that fail to meet the outlet requirement. Lines are drawn through all evaluated operating points to guide the eye.

1.37 kg. This demonstrates that correctly sizing the IAS system can make the fuel cycle more robust to conventionally less attractive scenarios, such as high protium percentages and low DIR fractions. More work can elucidate further the bounds of this robustness, and optimisation of the CD column may allow for a system that is more robust to fluctuations in feed stream compositions.

These results indicate that high DIR fractions may not be a requirement for ST-E1 and other fusion devices. Furthermore, it also shows a reasonably sized (<3.5 m) CD column would suffice for the current design point. These results culminate in the suggestion that 80% of the exhaust flow going into this system is feasible, further reducing the burden on the slower ISS, reducing the inventory in that system. The reduced inventory

may mean technologies beyond more commonly cited CD columns become options for the finer isotope separation in the ISS, which may have reduced duty.

4.2.4. Blanket inventory. Blanket tritium concentration has a critical influence on system performance, particularly because a threshold concentration must be exceeded before significant tritium extraction can occur, a phenomenon that is especially pronounced in pure lithium systems. An assumed extraction efficiency curve has been adopted, in which the blanket extraction efficiency only exceeds 1% at 100 ppb and reaches high values, 80%, only once the blanket concentration surpasses 1 ppm, as illustrated in figure 14. This relationship is implemented in PyFuel, computing the extraction efficiency dynamically, allowing for an assessment of the effects of blanket mass, flow rate, and the onset concentration where extraction begins.

The impact of this inventory on the startup tritium inventory is presented in figure ??, where the lithium mass is expressed as multiples of the blanket inventory, $M_{\mathrm{BL}} = 360\,000$ kg. Higher inventory levels led to higher startup inventories due to an extended incubation period required to achieve the minimum concentration. The analysis underscores the importance of reducing the total lithium inventory, not only from a safety standpoint but also to reduce the incubation period before extraction becomes effective. These results motivated the adoption of individual lithium loops per blanket segment, constraining the loop mass to $M_{\mathrm{loop}} \leqslant 5M_{\mathrm{BL}}$.

In addition, the blanket mass flow rate, initially chosen as 296 kg s^{-1}, has only a modest impact on the startup phase, as illustrated in figure 20(*a*). Higher flow rates become significant only for larger blanket masses, since the blanket residence time is directly proportional to the mass flow rate. As a result, the residence time[15] in the blanket is not the primary factor governing the initial startup response; instead, the blanket mass itself plays the dominant role. For smaller blanket masses, increasing the flow rate lowers the tritium concentration in the blanket, which diminishes the extraction efficiency and counteracts any benefits from faster processing.

To further evaluate the performance of the extraction system, the threshold concentration for extraction was investigated, as shown in figure 20(*b*), assuming $M_{\mathrm{loop}} = 5M_{\mathrm{BL}}$ and $\dot{m}_{BL} = 296$ kg s^{-1}. Among the parameters considered, this threshold concentration exerts the largest influence on the startup inventory. The figure presents both the startup inventory as a function of onset concentration and the corresponding average extraction efficiency for each system. Since the efficiency is constrained to 1% up to the onset threshold concentration, the efficiency of even the more sensitive extraction systems remains $\leqslant 30\%$. For the 20% bleed stream in ST-E1, this corresponds to an overall effective efficiency of $\leqslant 6\%$. Furthermore, a maximum in the startup inventory is observed for onset concentrations $\geqslant$3 ppm due to the extraction efficiency never exceeding 1% in this regime.

It is well established that pure lithium systems present additional challenges for tritium extraction, and consequently the startup inventory and the steady-state blanket inventory are adversely affected. However, these results indicate that a high ultimate extraction efficiency is not a strict requirement for an effective tritium extraction system. If a system can achieve a relatively modest extraction efficiency (e.g. 30%) at sufficiently low tritium concentrations, the impact on the inventories will be limited. Therefore, the primary design objective for such systems should be high sensitivity (i.e. low onset threshold concentration), rather than maximisation of the overall extraction efficiency.

Overall, it is clear that these sensitivities must be accounted for in tandem as further design develops, with actionable targets for the blanket design time to reduce the overall loop inventory. The tight coupling between the matter injection, plasma, vacuum pumping, and the overall Fuel Cycle is also well described here, with the outlet composition from the plasma, unsurprisingly, being a key determining factor for the overall fuel cycle architecture. The integration of the CODFISH results, in particular, highlights some simplifications to the system that can be made, suggesting that very high DIR percentages may be less desirable when accounting for the challenges associated with protium ingress into the fuelling systems. From these results the key drivers for ST-E1 will be the fuelling efficiency and the sensitivity of the tritium extraction system to the concentration of tritium in the liquid lithium, while DIR fraction and burn fraction will have a reduced effect with appropriate use of a CD column in the IAS and the limitations on the burn fraction that can be achieved for increasing values of R.

5. Conclusions

While the high fusion power and outboard-only breeding geometry of ST-E1 present challenges for the tritium fuel cycle, this study identifies a set of effective mitigation strategies and establishes an internally consistent, end-to-end fuel cycle baseline for the plant. Key characteristics of the fuel cycle have been explored, with selected subsystems modelled at higher fidelity and integrated into a plant-wide tritium inventory framework.

The analysis can be compared to the criteria listed in the introduction. In this paper, results have demonstrated that the systems interfacing the plasma provide favourable fuelling characteristics and that the vacuum system can manage the plasma exhaust with comfortable per-port pumping margins at $p_{\mathrm{div}} \approx 1$ Pa. Fast rebalancing requirements are compatible with a compact cryogenic distillation stage, maintaining a $\leqslant 0.8$ at.% protium constraint of up to at least 2 at.% protium at the inlet, without a significant penalty to startup inventory. The blanket inventory, which is often treated implicitly, is shown to be a potentially significant contributor to the total tritium

[15] Defined as $\frac{M_{loop}}{\dot{m}_{blanket}}$.

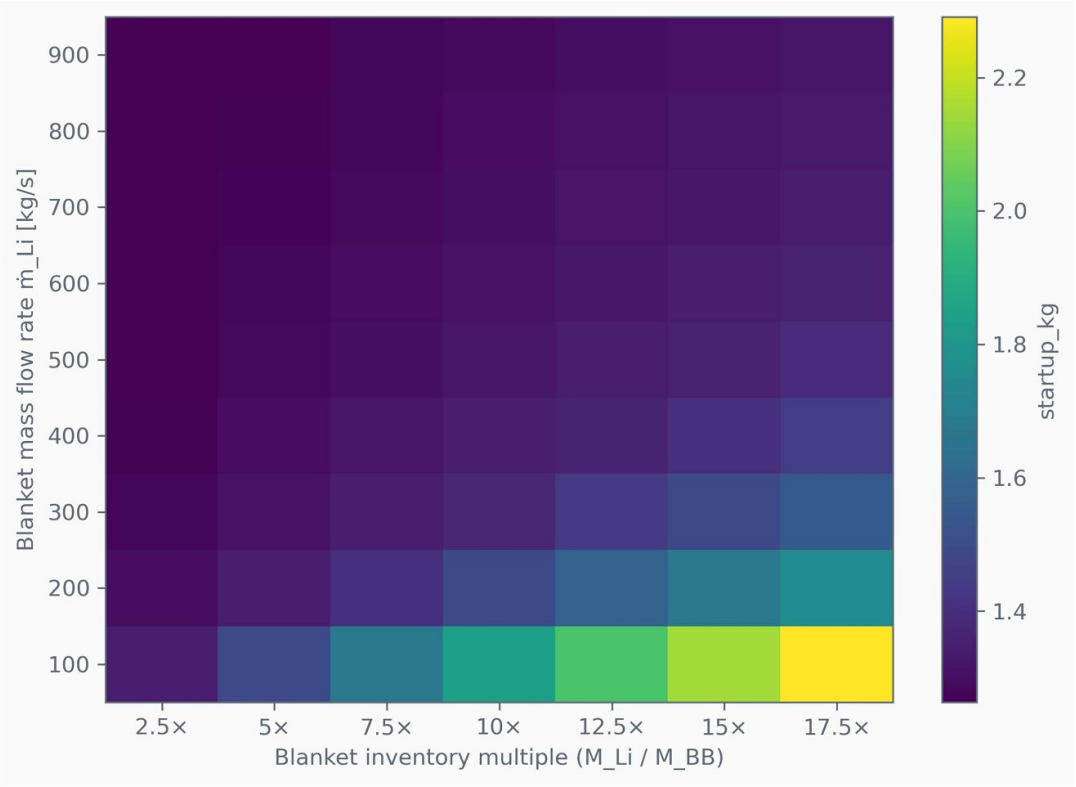

(a)

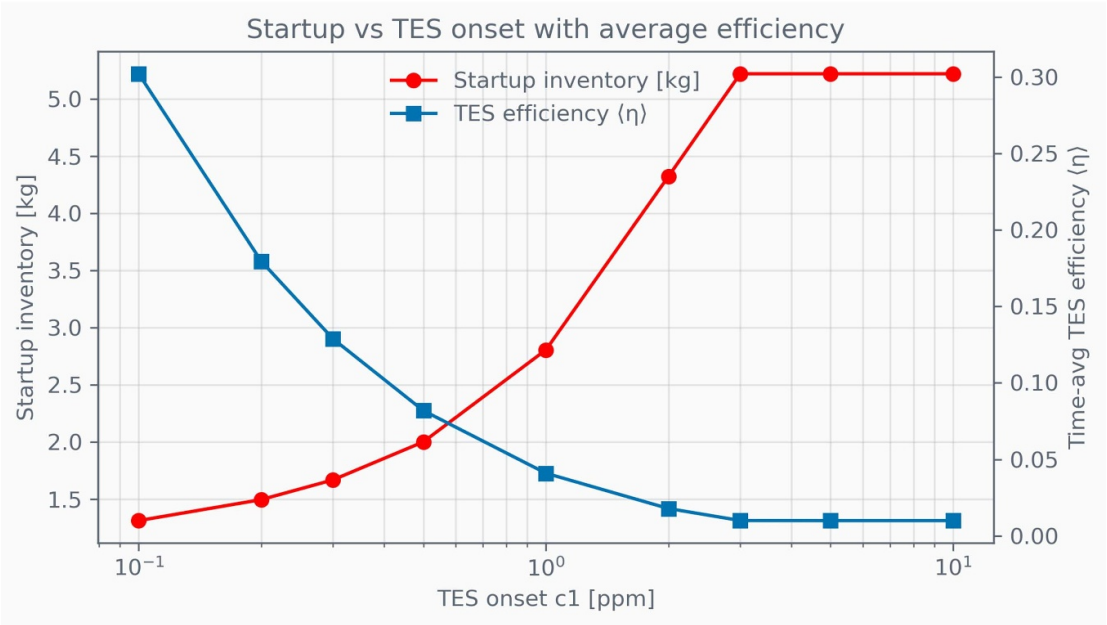

(b)

Figure 20. Blanket-loop sensitivity to startup tritium inventory. (a) Startup inventory as a function of blanket mass flow rate and blanket inventory and (b) sweep of different TES onset efficiencies.

inventory if not carefully controlled; reduction in mass and modularisation of the blanket therefore emerge as key mitigation strategies.

A central result of this work is that low-inventory fuel-cycle operation for ST-E1 is governed primarily by subsystem processing times and residence times, rather than by marginal improvements in the TBR. In particular, the onset concentration for tritium extraction from the blanket is identified as a dominant driver of both blanket and startup inventory, with substantially greater influence than the ultimate extraction

efficiency. For the extraction curves examined, increases in efficiency beyond approximately 30% provide diminishing benefits, reflecting the coupled reduction in tritium concentration. Similarly, the DIR fraction is shown to be a secondary driver of inventory, with minimal and somewhat negative effects observed in this study, while the protium inlet concentration exerts a stronger influence than the DIR fraction itself over the range considered.

Overall, the integrated tritium model achieves self-sufficiency with a low startup inventory and an acceptable doubling time, demonstrating the viability of the proposed fuel-cycle architecture for ST-E1. As the design matures, further work will be required to address integration under off-normal conditions, refine exhaust gas composition modelling, and improve chemistry control in the blanket. Throughout this development, safety considerations associated with lithium and tritium systems remain central to the design.

Acknowledgment

The authors thank M. Abdallah and S. Romanelli for their enlightening discussions at project inception. This work was undertaken as part of the US Department of Energy Milestone-based Fusion Development Program.

This research made use of the resources of the High Performance Computing Center at Idaho National Laboratory, which is supported by the Office of Nuclear Energy of the U.S. Department of Energy and the Nuclear Science User Facilities, United States under Contract No. SPP-24SP95. This manuscript has also been authored in part by UT-Battelle, LLC, under contract DE-AC05-00OR22725 with the US Department of Energy and Battelle Savannah River Alliance, LLC under Contract No. 89303321CEM000080 with the U.S. Department of Energy.

Data availability statement

TMAP8: The TMAP8 code is open source and available at https://github.com/idaholab/ TMAP8. The complete TMAP8 documentation, including instructions on how to get started, the verification and validation cases, and descriptions of all of TMAP8's capabilities, is available at https://mooseframework.inl.gov/TMAP8/index.html. OpenMC is avaialable at https://openmc.org/ and SPARTA is available at https://sparta.github.io/. Further data is available on request.

ORCID iDs

E. Yildirim 0000-0002-1903-1857
J. Naish 0009-0005-6763-490X
J. Trueba 0009-0007-6259-9281
S. Levine 0000-0002-9562-104X
A. Kumar 0000-0002-6026-5727
V.B. Gohani 0009-0001-0308-6298
M.K.E. Mohamed 0009-0008-8892-0827
A. Vorobev 0000-0002-6458-9390
L. Yang 0000-0002-1753-9462
P.C. Simon 0000-0001-7083-2628
A. Somers 0000-0001-9076-4992
C. Malone 0000-0003-1289-4681
H. Flynn 0000-0002-8444-1844
P. Rowell 0009-0007-8078-2119
T. Stahl 0000-0003-4470-8230
G.K. Larson 0000-0002-0753-1686
T.E. Gebhart 0000-0001-8259-6095
N. Adhikari 0000-0002-1345-0911

References

[1] Willis J. *et al* 2026 Tokamak Energy's pre-concept design for a fusion power plant: an overview of ST-E1 *Nucl. fusion* **66** 086001
[2] Wilson C.L., McNamara S.A.M., Ginsberg M.J., Willis J., Astbury J., Yildirim E., Hinton N. and Maartensson E.N.J. 2026 Design scoping and systems modelling of ST-E1 using the PyTOK whole-plant code *Nucl. fusion* **66** 086002
[3] Willis J. *et al* (the ST-E1 Team) 2026 Maintenance strategy, structural design, and site layout of the ST-E1 fusion power plant *Nucl. fusion* **66** 086006
[4] Giancarli L.M. *et al* 2024 Status of the ITER TBM Program and overview of its technical objectives *Fusion Eng. Des.* **203** 114424
[5] Hernández F.A. *et al* 2019 Advancements in the helium-cooled pebble bed breeding blanket for the EU DEMO: holistic design approach and lessons learned *Fusion Sci. Technol.* **75** 352–64
[6] Liu S. *et al* 2022 Design of the water-cooled ceramic breeder blanket for CFETR *Fusion Eng. Des.* **177** 113059
[7] Pearson R., Baus C., Konishi S., Mukai K., D'Angio A. and Takeda S. 2022 Overview of Kyoto fusioneering's SCYLLA© ('self-cooled yuryo lithium-lead advanced') blanket for commercial fusion reactors *IEEE Trans. Plasma Sci.* **50** 4406–12
[8] Smith D.L. *et al* 1984 *Blanket Comparison and Selection Study: Final Report* ANL/FPP-84-1 Argonne National Laboratory ANL/FPP-84-1
[9] Romano P.K., Horelik N.E., Herman B.R., Nelson A.G., Forget B. and Smith K. 2015 OpenMC: a state-of-the-art Monte Carlo code for research and development *Ann. Nucl. Energy* **82** 90–97
[10] Shimwell J., Lilley S., Morgan L., Packer L., Kovari M., Zheng S. and McMillan J. 2016 Reducing beryllium content in mixed bed solid-type breeder blankets *Fusion Eng. Des.* **109-111** 1564–8
[11] Gan Y., Kamlah M., Riesch-Oppermann H., Rolli R. and Liu P. 2011 Crush probability analysis of ceramic breeder pebble beds under mechanical stresses *J. Nucl. Mater.* **417** 706–9
[12] Yang A., Xu Y., Zhu K. and Zhou Q. 2025 Study on the structure of Li2TiO3-Li4SiO4 tritium breeder and its performance under thermal cycle loading with compression pressure *J. Nucl. Mater.* **609** 155726
[13] Chandrasekhar K., Wilson C.L., Levine S.M., Irukuvarghula S., Naish J.D., Godhani V.B., Márquez A.A. and Loughlin M.J. 2026 Nuclear technology considerations and neutronics for the ST-E1fusion power plant *Nucl. fusion* **66** 086003
[14] Zinkle S.J. and Busby J.T. 2009 Structural materials for fission & fusion energy *Mater. Today* **12** 12–19
[15] Chopra O.K., Smith D.L., Tortorelli P.F., DeVan J.H. and Sze D.K. 1985 Liquid-metal corrosion *Fusion Technol.* **8** 1956–69
[16] Pint B.A., Pawel S.J., Howell M., Moser J.L., Garner G.W., Santella M.L., Tortorelli P.F., Wiffen F.W. and Distefano

J.R. 2009 Initial characterization of V-4Cr-4Ti and MHD coatings exposed to flowing Li *J. Nucl. Mater.* **386** 712–5
[17] Zinkle S.J. and Ghoniem N.M. 2000 Operating temperature windows for fusion reactor structural materials *Technical Report* (available at: www.elsevier.com/locate/fusengdes)
[18] Shimada M. 2020 Tritium transport in fusion reactor materials *Comprehensive Nuclear Materials* 2nd edn (Elsevier) pp 251–73
[19] Wipf H. 2001 Solubility and diffusion of hydrogen in pure metals and alloys *Phys. Scr.* **T94** 43
[20] Bhattacharya A., Zinkle S.J., Henry J., Levine S.M., Edmondson P.D., Gilbert M.R., Tanigawa H. and Kessel C.E. 2022 Irradiation damage concurrent challenges with RAFM and ODS steels for fusion reactor first-wall/blanket: a review *J. Phys. Energy* **4** 034003
[21] Smith D., Chung H., Loomis B. and Tsai H.-C. 1996 Reference vanadium alloy V-4Cr-4Ti for fusion application *J. Nucl. Mater.* **233-237** 356–63
[22] Nagasaka T. and Muroga T. 2020 Vanadium for Nuclear Systems *Comprehensive Nuclear Materials* (Elsevier) pp 1–18
[23] Pint B.A., DiStefano J.R. and Tortorelli P.F. 2003 High temperature compatibility issues for fusion reactor structural materials *Fusion Sci. Technol.* **44** 433–40
[24] Chaia N., Mathieu S., Cozzika T., Rouillard F., Desgranges C., Courouau J.L., Petitjean C., David N. and Vilasi M. 2013 An overview of the oxidation performance of silicide diffusion coatings for vanadium-based alloys for generation IV reactors *Corros. Sci.* **66** 285–91
[25] Mohamed M.K.E. *et al* 2026 Thermal management and net-power evaluation of the ST-E1 fusion power plant *Nucl. fusion* **66** 086005
[26] Nitti F.S., Maestre J., Dezsi T., Gordeev S., Holstein N., Brenneis B., Buligins L., Molla J. and Ibarra A. 2025 The lithium systems of the IFMIF-DONES facility *Nucl. Fusion* **65** 12
[27] Muroga T., Tanaka T., Li Z., Sagara A. and Sze D.-K. 2007 Tritium control for flibe/V-alloy blanket system *Fusion Sci. Technol.* **52** 682–6
[28] Garcia-Diaz B.L. *et al* Technology development and materials research to enable a sustainable D-T fusion energy fuel cycle *Technical Report* 1
[29] Teprovich J.A., Colon Mercado H.R., Olson L., Ganesan P., Babineau D. and Garcia-Diaz B.L. 2019 Electrochemical extraction of hydrogen isotopes from Li/LiT mixtures *Fusion Eng. Des.* **139** 1–6
[30] Humrickhouse P.W. and Merrill B.J. 2018 Tritium aspects of the fusion nuclear science facility *Fusion Eng. Des.* **135** 302–13
[31] Morgan G.A. and Hodge B.J. 2016 Performance testing of a prototype Pd-Ag diffuser *Technical Report*
[32] Yoshida H., Konishi S. and Naruse Y. 1983 Preliminary design of a fusion reactor fuel cleanup system by the palladium-alloy membrane method *Nucl. Technol. - Fusion* **3** 471–84
[33] Piet S.J. 1985 Safety evaluation of the blanket comparison and selection study *Fusion Technol.* **8** 77–89
[34] American Nuclear Society 2025 *Liquid metal fire protection in LMR plants* ANSI/ANS-54.8-2025 American National Standards Institute
[35] D'Ovidio G., Martín-Fuertes F., Marugán J.C., Bermejo S. and Nitti F.S. 2023 Lithium fire protection design approach in IFMIF-DONES facility *Fusion Eng. Des.* **189** 113446
[36] Whyte D., Delaporte-Mathurin R., Ferry S. and Meschini S. 2023 Tritium burn efficiency in deuterium-tritium magnetic fusion *Nucl. Fusion* **63** 126019
[37] Jackson G.L., Chan V.S. and Stambaugh R.D. An analytic expression for the tritium burnup fraction in burning-plasma devices *Technical Report*
[38] Abdou M., Riva M., Ying A., Day C., Loarte A., Baylor L.R., Humrickhouse P., Fuerst T.F. and Cho S. 2021 Physics and technology considerations for the deuterium-tritium fuel cycle and conditions for tritium fuel self sufficiency *Nucl. Fusion* **61** 013001
[39] Baylor L.R., Jernigan T.C., Parks P.B., Antar G., Brooks N.H., Combs S.K., Fehling D.T., Foust C.R., Houlberg W.A. and Schmidt G.L. 2007 Comparison of deuterium pellet injection from different locations on the DIII-D tokamak *Nucl. Fusion* **47** 1598–606
[40] Janky F., Fable E., Treutterer W. and Zohm H. 2017 Simulation of burn control for DEMO using ASTRA coupled with Simulink *Fusion Eng. Des.* **123** 555–8
[41] Houlberg W.A., Iskra M.A., Howe H.C. and Attenberger S.E. 1979 PELLET: a computer routine for modeling pellet fueling in tokamak plasmas *Technical Report* (Oak Ridge National Laboratory (ORNL))
[42] McNamara S.A.M. *et al* 2026 Physics basis for the reference flat-top plasma scenario in the ST-E1 fusion power plant *Nucl. fusion* **66** 086008
[43] Koechl F., Pegourie B., Matsuyama A., Nehme H., Waller V., Frigione D., Garzotti L. and Kamelander P. 2012 Modelling of pellet particle ablation and deposition: the hydrogen pellet injection code HPI2 *Technical Report* (available at: www.iop.org/Jet)
[44] Reiter C., Fietz S., Borsuk A., Moeller S. and Lang P.T. 2018 Physical constraints on the design of the DEMO pellet fueling system *Proc. 30th Symp. on Fusion Technology (SOFT)*
[45] Robinson M. *et al* 2026 Power and particle exhaust in the ST-E1 Fusion Power Plant *Nucl. fusion* **66** 086011
[46] Gallis M.A., Torczynski J.R., Plimpton S.J., Rader D.J. and Koehler T. 2014 Direct simulation Monte Carlo: the quest for speed *AIP Conf. Proc.* **1628** 27–36
[47] Day C. and Murdoch D. 2008 The ITER vacuum systems *J. Phys.: Conf. Ser.* **114** 773–8
[48] Haas H., Day C., Mack A. and Murdoch D.K. 2003 Performance tests of the ITER model pump *Fusion Eng. Des.* **69** 91–95
[49] Pearce R and Worth L 2024 *ITER Vacuum Handbook: Appendices and Attachments* ITR-24-012 ITER Organization
[50] Adhikari N., Gebhart T.E. and Baylor L.R. 2025 Computational study of a cryopump design for fusion exhaust gas purification using direct simulation Monte Carlo *IEEE Trans. Plasma Sci.* 1–6
[51] Gebhart T.E., Adhikari N., Quinlan B., Baylor L.R., Marcus C., Matiauda S. and Ottinger D. 2025 Preliminary testing of a continuous cryopump for primary fusion device pumping and direct internal recycling *IEEE Trans. Plasma Sci.* 1–7
[52] Somers A., Malone C., Flynn H.B., RowellIV P.A., LarsenIII G.K. 2025 Effects of target protium content on steady state isotope rebalancing and protium removal distillation column operation (available at: www.osti.gov/biblio/2555694)
[53] Friday J.R. and Smith B.D. 1964 An analysis of the equilibrium stage separations problem-formulation and convergence *AIChE J.* **10** 698–706
[54] Wang J.C. and Henke G.E. 1966 Tridiagonal Matrix for Distillation *Hydrocarbon Process.* **45** 155–63
[55] Simon P.-C.A. *et al* 2025 MOOSE-based tritium migration analysis program, version 8 (TMAP8) for advanced open-source tritium transport and fuel cycle modeling *Fusion Eng. Des.* **214** 114874
[56] Shimada M., Simon P.-C.A., Icenhour C.T. and Singh G. 2024 Toward a high-fidelity tritium transport modeling for retention and permeation experiments *Fusion Eng. Des.* **203** 114438

[57] Yang L., Simon P.C.A., Yildirim E., Trueba J., Robinson M. and Shimada M. 2026 Multiscale assessment of tritium behavior in preliminary fusion pilot plant design using surrogate models in TMAP8 *Nucl. fusion* Submitted
[58] Tanabe T. 1995 Surface Barrier for Tritium Permeation *Fusion Technol.* **28** 1278–83
[59] 1996 Safety of magnetic fusion facilities: requirements *Technical Report* DOE-STD-6002-96 (U.S. Department of Energy)
[60] 2015 Tritium handling and safe storage *Technical Report* DOE-STD-1129-2015 (U.S. Department of Energy)
[61] Preparation Guide for U.S. Department of Energy Nonreactor Nuclear Facility Safety Analyses 2014 *Technical Report* DOE-STD-3009-2014 (U.S. Department of Energy)
[62] Department of Energy 2016 Nuclear material control and accountability *Technical Report* DOE O 474.2A (U.S. Department of Energy)
[63] 2019 Nuclear materials control and accountability *Technical Report* DOE-STD-1194-2019 (U.S. Department of Energy)
[64] Meschini S., Ferry S.E., Delaporte-Mathurin R. and Whyte D.G. 2023 Modeling and analysis of the tritium fuel cycle for ARC- and STEP-class D-T fusion power plants *Nucl. Fusion* **63** 126005
[65] Malone C.R., Flynn H.B., Somers A.D., Rowell P.A. and Larsen G.K. 2024 Approach to startup inventory for viable commercial fusion power plant *Fusion Eng. Des.* **206** 114563
[66] Candido L., Alberghi C., Arena P., Moro F., Noce S., Utili M. and Zucchetti M. 2023 Tritium transport in WCLL outboard breeding blanket of EU-DEMO reactor under pulsed plasma operation *Fusion Sci. Technol.* **79** 1197–207
[67] Candido L., Alberghi C., Moro F., Noce S., Testoni R., Utili M. and Zucchetti M. 2021 A novel approach to the study of magnetohydrodynamic effect on tritium transport in WCLL breeding blanket of DEMO *Fusion Eng. Des.* **167** 112334
[68] Larsen G.K., Flynn H.B. and Rowell P.A. 2023 Savannah River National Laboratory–General Fusion 2023 INFUSE report *Technical Report*
[69] Arias A.A., Schmierer E.N., Gettemy D., Howard D.W., Wermer J.R. and Tuggle D.G. 2005 Thermal cycling absorption process (TCAP): instrument and simulation development status at Los Alamos National Laboratory *Fusion Sci. Technol.* **48** 159–62
[70] Day C. and Giegerich T. 2013 The direct internal recycling concept to simplify the fuel cycle of a fusion power plant *Fusion Eng. Des.* **88** 616–20